Influence of imperfections on the stability of a multi-disc friction system

Alexy Mercier, Louis Jezequel

Influence of imperfections on the stability of a multi-disc friction system

Alexy MERCIER[1]

Post-doctoral researcher, LTDS, École Centrale Lyon, Ecully

Louis JEZEQUEL

Dean professor, LTDS, École Centrale Lyon, Ecully

Abstract

This paper studies the impact of geometrical imperfections (gaps in the links, center distance, inclination angle, etc.) on the stability and the dynamic behavior of mechanical systems exhibiting friction-induced vibrations (braking systems, clutches, etc.). It comes further to two papers relating to improved modeling of friction and separation at the interface of a rotor-stator system. The latter is a phenomenological model which is composed of an embedded beam on which a disc is mounted, called the stator, in contact with another disc called the rotor. The phenomenological mechanical system used in this paper is a new version of the latter model taking into account some of the geometrical imperfections present in real mechanical sytems. In the proposed model, the rotor and stator discs have the ability to move radially thanks to the gaps in the links. The inclination angle of the rotor disc and a center distance between the stator and the rotor discs are also introduced. The inclusion of these three geometrical imperfections induces additional complex phenomena that have a strong impact on the stability and dynamic behaviour of the mechanical system, because the coupling of the imperfections with the rotor rotation gives rise to a non-autonomous dynamical system. Consequently, stability studies of fixed points must be replaced by stability studies of periodic orbits involving the construction of a monodromy matrix. In conclusion, significant differences in the values of the bifurcation point and the levels of the associated instabilities can be observed, unlike in a study that does not take geometrical imperfections into account.

Key words: Friction-induced vibrations, nonlinear phenomena, geometrical imperfections, stability of fixed points, orbital stability, temporal integrations.

1. Introduction

Mechanical systems exhibiting friction-induced vibration instabilities are commonly encountered by design engineers working in industry. The elementary design of systems presenting this type of instability is often very similar (stationary and rotative part), although they can be difficult to compare in some cases. There are many examples of such systems, the best known of which are braking systems (automotive [1–4], aeronautics [5–9], railway [10]), on which many works have been carried out, and other systems like those for clutches [11, 12] or simplified mechanical systems [13–21]. The mechanisms or physical phenomena at the origin of these vibrations, which are detrimental to structures (damage, rupture, premature wear, etc.), have been studied for many years by means of experimental and numerical simulations. From all the research work relating to friction-induced vibrations, two main mechanisms have been evidenced to explain their appearance. The first is called stick-slip and is related to the tribological characteristics of the materials in contact. The first works to refer to the stick-slip phenomenon were those of [22]. Further works by [23–26] also helped to explain this phenomenon. Other, more applied studies have been carried out with models presenting this phenomenon in [13, 27–29]. Physically, the stick-slip phenomenon appears when the adhesion (static) and friction (dynamic) coefficients are different. In this case, the tangential force depends on the velocity relative to the

Email addresses: alexy.mercier@ec-lyon.fr (Alexy MERCIER), louis.jezequel@ec-lyon.fr (Louis JEZEQUEL)

interface. This dependence can be continuous or discontinuous. In the discontinuous case, a jump from the boundary of the adhesion cone to that of the friction cone appears. In the continuous case, a decrease in the friction coefficient is achieved by following a certain law, as in the works of [30–34]. The second mechanism is called a sprag-slip and is linked to the geometric characteristics of the parts. It was put forward in the work by [35] to explain brake squeal noises. Physically, this phenomenon is due to the coupling between the normal and tangential forces (sprag phase), then a release from the latter (slip phase). When the sprag-slip theory was generalized, the notion of mode coupling thus appeared. Theoretically, sprag-slip requires at least two degrees of freedom (tension-compression and bending). Many additional studies relating to mode coupling have been carried out [36–39].
This paper follows on from studies of phenomena located at the interface of the rotor and stator discs of a very simplified phenomenological model [40, 41]. The mechanical system associated with this model consists of an embedded beam on which a stator disc is mounted. Another disc called a rotor, with a rotation velocity, is in frictional contact with the stator disc. According to the values of the parameters and in particular the coefficient of friction at the rotor-stator interface, the friction at the interface can induce a vibratory instability called Whirl mode. This instability corresponds to the coalescence of the two bending modes of the beam. A damping is often introduced into models in order to obtain realistic levels, due to a lack of nonlinear phenomena in the modeling. In the two papers cited, two improvements were analyzed. The first consisted of a better description of the velocities field relating to the rotor-stator interface. This first improvement makes it possible to introduce a damping due to friction at the interface which is proportional to the pressure at the interface and inversely proportional to the velocity rotation of the rotor disc. The second improvement consisted in taking into account the separation at the interface, something which is often neglected in order to simplify the calculations. The separation at the interface gives rise to a new mode called Squeal that is not detectable by fixed point stability analyses because it corresponds to a change of the basin of attraction.
In this paper and based on the above improvements, a new version of the described phenomenological model is studied. Gaps in the links associated with the stator and rotor discs are modeled, which induces a division of the discs into two parts. Further, a center distance between the axles of the stator and rotor discs is taken into account. Last, an inclination angle of the rotor disc is introduced into the modeling. These three geometrical imperfections are most often not taken into account so as not to complicate modeling or lengthen calculation times. However, these improvements make it possible to better model the design of most mechanical systems. Indeed, in many mechanical systems, the discs are mounted in sliding links with other parts and there is thus a gap in the link. Moreover, as the geometry is not perfect, a center distance and a difference in axis between the stationary and rotating parts may exist. The coupling of these three geometrical imperfections with the rotor disc rotation induces a periodic excitation and the associated dynamical system becomes non-automonous. The usual studies of the stability of fixed points are in some cases no longer possible and so the main aim of this study is to analyze the influence of the three imperfections on stability with the help of the phenomenological model. First, the phenomenological model and the associated hypotheses will be presented. Next, the equations of motion will be written using a Lagrangian approach. Finally, a parametric study will be carried out including determination and stabiliy studies of fixed points and periodic orbits.

2. Model presentation and main hypotheses

The phenomenological model studied is represented in figure (1) and the associated parameters are given in table (1). This is a mechanical system moving in the Euclidian space $\mathbb{E}$ and whose structure is composed of an embedded beam, a rotor disc and a stator disc. In order to simplify the mechanical problem, the small perturbations hypothesis is made.

2.1. Beam

This first main set is a deformable beam named b, occuping domain $\Omega_b(t) \subset \mathbb{E}$ at each time $t \in \mathbb{T} = [0, t_{max}]$. The frame on which the beam is fixed is chosen as the reference inertial frame and is designated by R_0. The point O chosen in the embedding and the basis $\mathcal{B}_0$ make it possible to build the cartesian coordinate system $\mathcal{R}_0 = (O, \boldsymbol{e_1}, \boldsymbol{e_2}, \boldsymbol{e_3})$. The displacement field of the beam is defined as $\boldsymbol{u^b} : \Omega_b(t) \times \mathbb{T} \longrightarrow \mathbb{R}^3, (\boldsymbol{x}, t) \longmapsto \boldsymbol{u}(\boldsymbol{x}, t)$ and must verify $\boldsymbol{u^b}(\boldsymbol{0}, t) = \boldsymbol{0} \ \ \forall t \in \mathbb{T}$. In order to simplify the mechanical problem associated with the beam, new hypotheses are made:

- The beam is considered infinitely rigid in tension, compression and torsion.

- The *Euler-Bernoulli* hypothesis ($L \gg b$ and $L \gg h$):

$$\forall \boldsymbol{x_G} = x\,\boldsymbol{e_1} \in \mathbb{R}^3,\ \ \boldsymbol{u^b}(\boldsymbol{x},t) = \boldsymbol{u^b}(\boldsymbol{x_G},t) + \boldsymbol{\theta^b}(\boldsymbol{x_G},t) \wedge (\boldsymbol{x}-\boldsymbol{x_G}) = \begin{bmatrix} 0 \\ u_2^b(\boldsymbol{x_G},t) \\ u_3^b(\boldsymbol{x_G},t) \end{bmatrix} + \begin{bmatrix} 0 \\ -\frac{\partial u_3^b(\boldsymbol{x_G},t)}{\partial x} \\ -\frac{\partial u_2^b(\boldsymbol{x_G},t)}{\partial x} \end{bmatrix} \wedge \begin{bmatrix} 0 \\ y \\ z \end{bmatrix} \tag{1}$$

  where: $\boldsymbol{x_G} \in \mathbb{R}^3$, is the position vector associated with the center of the section. This is a movement of rigid bodies of each section with small strains from where $\boldsymbol{\theta^b}(\boldsymbol{x_G},t) = \frac{\partial \boldsymbol{u^b}(\boldsymbol{x_G},t)}{\partial x}$.

It should also be specified that the geometrical parameters, in particular those of the noted beam b, were chosen to satisfy the assumption of the model and in particular that of textit Euler-Bernoulli. For example, the external force F_{ext}, must induce displacements at the end of the beam satisfying this last hypothesis. The spatial approximation of the displacement field $\boldsymbol{u}$ is carried out using the *Rayleigh-Ritz* method. This method allows one to build an approximation sub-space of finite dimension called V_b^h included in the *Sobolev* space $V_b = H_0^1(\Omega_b(t),\mathbb{R}^3)$ (null fieds in $\boldsymbol{x} = \boldsymbol{0}$). Therefore, the approximated displacements and velocities fields of beam b are written:

$$\forall \boldsymbol{x} \in \Omega_b(t)\ \ \forall t \in \mathbb{T}, \begin{cases} \tilde{\boldsymbol{u}}^{\boldsymbol{b}}(\boldsymbol{x},t) = \boldsymbol{N}(\boldsymbol{x})\,\boldsymbol{q^b}(t) \\ \dot{\tilde{\boldsymbol{u}}}^{\boldsymbol{b}}(\boldsymbol{x},t) = \boldsymbol{N}(\boldsymbol{x})\,\dot{\boldsymbol{q}}^{\boldsymbol{b}}(t) \end{cases} \text{ and } \begin{cases} \tilde{\boldsymbol{\theta}}^{\boldsymbol{b}}(\boldsymbol{x},t) = \dfrac{d\,\boldsymbol{N}(\boldsymbol{x})}{d\,x}\,\boldsymbol{q^b}(t) \\ \dot{\tilde{\boldsymbol{\theta}}}^{\boldsymbol{b}}(\boldsymbol{x},t) = \dfrac{d\,\boldsymbol{N}(\boldsymbol{x})}{d\,x}\,\dot{\boldsymbol{q}}^{\boldsymbol{b}}(t) \end{cases} \tag{2}$$

with:

- $\boldsymbol{q^b}(t) = \begin{bmatrix} 0 \\ q_1(t) \\ q_2(t) \end{bmatrix} \in \mathbb{R}^3$, the vector containing the generalized coordinates $q_1(t)$ and $q_2(t)$ which correspond to the displacements of point O_1 (extremity of the beam) following directions y and z and measured in inertial frame R_0 thanks to $\mathcal{R}_0 = (O, \boldsymbol{e_1}, \boldsymbol{e_2}, \boldsymbol{e_3})$.
- $\boldsymbol{N}(\boldsymbol{x}) \in \mathcal{M}_{3,3}(\mathbb{R})$, the matrix containing the shape functions.

2.2. Stator and rotor discs

At the end of the beam (point O_1), a stator disc is mounted, denoted s and composed of two parts. The first, denoted s_1, is fixed to beam b and point O_1 is the mass center. The second, denoted s_2, is a plate mounted in the slide link with s_1 and can have a relative movement measured in the inertial frame R_1 as reference inertial of the cartesian coordinate system $\mathcal{R}_1(t) = \left(O_1(t), \boldsymbol{e_1^{s_1}}(t), \boldsymbol{e_2^{s_1}}(t), \boldsymbol{e_3^{s_1}}(t)\right)$. This relative displacement is given by the generalized coordinate, denoted $q_5(t)$, at each time $t \in \mathbb{T}$. The passage from frame R_1 to R_0 induces a change of cartesian system and is associated with the following affine application:

$$\boldsymbol{f}_{\mathcal{R}_1(t),\mathcal{R}_0} : \mathbb{R}^3 \longrightarrow \mathbb{R}^3, \boldsymbol{x'}(t) \longmapsto \boldsymbol{x}(t) = \boldsymbol{C}_{O,O_1(t)}(t) + \boldsymbol{P}_{\mathcal{B}_1(t),\mathcal{B}_0}(t)\,\boldsymbol{x'}(t) \tag{3}$$

with:

- $\boldsymbol{C}_{O,O_1(t)}(t) = \boldsymbol{OO_1}(t) = \begin{bmatrix} L + \frac{e}{2} \\ q_1(t) \\ q_2(t) \end{bmatrix}_{\mathcal{B}_0}$, the origin changing (translation).
- $\boldsymbol{P}_{\mathcal{B}_1,\mathcal{B}_0}(t) = \begin{bmatrix} \boldsymbol{e_1^{s_1}}(t) & \boldsymbol{e_2^{s_1}}(t) & \boldsymbol{e_3^{s_1}}(t) \end{bmatrix}_{\mathcal{B}_1(t),\mathcal{B}_0} = \begin{bmatrix} \cos(\frac{2\,q_1(t)}{L})\cos(\frac{2\,q_2(t)}{L}) & -\sin(\frac{2\,q_1(t)}{L}) & -\cos(\frac{2\,q_1(t)}{L})\sin(\frac{2\,q_2(t)}{L}) \\ \cos(\frac{2\,q_2(t)}{L})\sin(\frac{2\,q_1(t)}{L}) & \cos(\frac{2\,q_1(t)}{L}) & -\sin(\frac{2\,q_1(t)}{L})\sin(\frac{2\,q_2(t)}{L}) \\ \sin(\frac{2\,q_2(t)}{L}) & 0 & \cos(\frac{2\,q_2(t)}{L}) \end{bmatrix}_{\mathcal{B}_1(t),\mathcal{B}_0}$, the passage matrix associated with the basic changing ($\mathcal{B}_1(t)$ to $\mathcal{B}_0$).

As for stator disc s, then rotor disc denoted r is also composed of two parts. The first, denoted r_1, has a constant inclination angle β with respect to direction z and rotates at a rotation velocity ω_r. More, r is kept in contact (interface $(s_2 - r_2)$) with the stator disc s by an external force F_{ext}. These two parameters (ω_r and F_{ext}) were considered constant since their influences on the dynamic behavior of this system have already been studied in [40, 41]. The existence of this inclination angle β implies that the axes of stator s_1 and rotor s_2 discs are no longer parallel and coincident. Consequently, it is rotating around direction x'' (different from x') with a velocity rotation $\omega_r = \theta_r\, t$, $t \in \mathbb{T}$ and can have an axial displacement (following direction x) represented by the generalized coordinate $q_3(t)$ in the reference inertial frame R_0. A center distance, denoted d, between the axes of stator s_1 and rotor r_1 may also exist. This center distance d implies that the axes of stator s_1 and rotor r_1 discs are no longer the same if the angle of inclination β is zero. When angle β is different from zero, the existence of a center distance d amplifies the geometric imperfection: the axes are not parallel and not confused. The second, denoted r_2, is a plate mounted in the slide link with r_1 and can have a relative movement measured in inertial frame R_2 as reference inertial of the cartesian coordinate system $\mathcal{R}_2(t) = \left(O_3(t), \boldsymbol{e_1}^{r_1}(t), \boldsymbol{e_2}^{r_1}(t), \boldsymbol{e_3}^{r_1}(t)\right)$. This relative displacement is given by the generalized coordinate, denoted $q_6(t)$. The passage from frame R_2 to R_0, a change of cartesian system, is done by the following affine application:

$$f_{\mathcal{R}_2(t),\mathcal{R}_0} : \mathbb{R}^3 \longrightarrow \mathbb{R}^3, \boldsymbol{x''}(t) \longmapsto \boldsymbol{x}(t) = \boldsymbol{C}_{O,O_3(t)}(t) + \boldsymbol{P}_{\mathcal{B}_2(t),\mathcal{B}_0}(t)\, \boldsymbol{x''}(t) \tag{4}$$

with:

- $\boldsymbol{C}_{O,O_3(t)}(t) = \boldsymbol{OO_3}(t) = \begin{bmatrix} L + \frac{3}{2}\, e + q_3(t) \\ 0 \\ 0 \end{bmatrix}_{\mathcal{B}_0}$, the origin changing.
- $\boldsymbol{P}_{\mathcal{B}_2(t)\to\mathcal{B}_0}(t) = \left[\boldsymbol{e_1}^{r_1}(t) \quad \boldsymbol{e_2}^{r_1}(t) \quad \boldsymbol{e_3}^{r_1}(t)\right]_{\mathcal{B}_2(t),\mathcal{B}_0} = \begin{bmatrix} \cos(\beta) & -\sin(\beta)\cos(\theta_r(t)) & \sin(\beta)\sin(\theta_r(t)) \\ \sin(\beta) & \cos(\beta)\cos(\theta_r(t)) & -\cos(\beta)\sin(\theta_r(t)) \\ 0 & \sin(\theta_r(t)) & \cos(\theta_r(t)) \end{bmatrix}_{\mathcal{B}_2(t),\mathcal{B}_0}$, the passage matrix associated with the basic changing ($\mathcal{B}_2(t)$ to $\mathcal{B}_0$).

In order to simplify the mechanical problem, the following hypotheses are made:

- The stator and rotor discs are considered undeformable:

$$\forall t \in \mathbb{T}, \quad \begin{cases} \dot{\boldsymbol{u}}^{s_1}_{/R_0}(\boldsymbol{x}, t) = \dot{\boldsymbol{u}}^{s_1}_{/R_0}(\boldsymbol{x_{O_1}}, t) + \dot{\boldsymbol{\theta}}^{s_1}_{/R_0}(\boldsymbol{x_{O_1}}, t) \wedge (\boldsymbol{x} - \boldsymbol{x_{O_1}}) \quad \forall \boldsymbol{x} \in \Omega_{s_1}(t) \\ \dot{\boldsymbol{u}}^{s_2}_{/R_0}(\boldsymbol{x}, t) = \dot{\boldsymbol{u}}^{s_1}_{/R_0}(\boldsymbol{x_{O_1}}, t) + \dot{\boldsymbol{u}}^{s_2}_{/R_1}(\boldsymbol{x_{O_2}}, t) + \dot{\boldsymbol{\theta}}^{s_1}_{/R_0}(\boldsymbol{x_{O_1}}, t) \wedge (\boldsymbol{x} - \boldsymbol{x_{O_1}}) \quad \forall \boldsymbol{x} \in \Omega_{s_2}(t) \\ \dot{\boldsymbol{u}}^{r_1}_{/R_0}(\boldsymbol{x}, t) = \dot{\boldsymbol{u}}^{r_1}_{/R_0}(\boldsymbol{x_{O_3}}, t) + \dot{\boldsymbol{\theta}}^{r_1}_{/R_0}(\boldsymbol{x_{O_3}}, t) \wedge (\boldsymbol{x} - \boldsymbol{x_{O_3}}) \quad \forall \boldsymbol{x} \in \Omega_{r_1}(t) \\ \dot{\boldsymbol{u}}^{r_2}_{/R_0}(\boldsymbol{x}, t) = \dot{\boldsymbol{u}}^{r_1}_{/R_0}(\boldsymbol{x_{O_3}}, t) + \dot{\boldsymbol{u}}^{r_2}_{/R_2}(\boldsymbol{x_{O_4}}, t) + \dot{\boldsymbol{\theta}}^{r_1}_{/R_0}(\boldsymbol{x_{O_3}}, t) \wedge (\boldsymbol{x} - \boldsymbol{x_{O_3}}) \quad \forall \boldsymbol{x} \in \Omega_{r_2}(t) \end{cases} \tag{5}$$

Parameter name	Notation	Value	Unit
System density	ρ	7800	$kg.m^{-3}$
Thickness of the beam following y	b	$2.5\,10^{-2}$	m
Thickness of the beam following z	h	$3\,10^{-2}$	m
Beam length	L	$2\,10^{-1}$	m
Contact stiffness per area unit	k	$2.5\,10^{9}$	$N.m^{-3}$
Young modulus	E	$210\,10^{9}$	Pa
Coulomb modulus	G	$81\,10^{9}$	Pa
Thickness of the rotor and stator discs	e	$1\,10^{-2}$	m
Radius of the stator	R_s	$7.5\,10^{-2}$	m
Radius of the rotor	R_r	$+\infty$	m

Table 1: Values of constant parameters

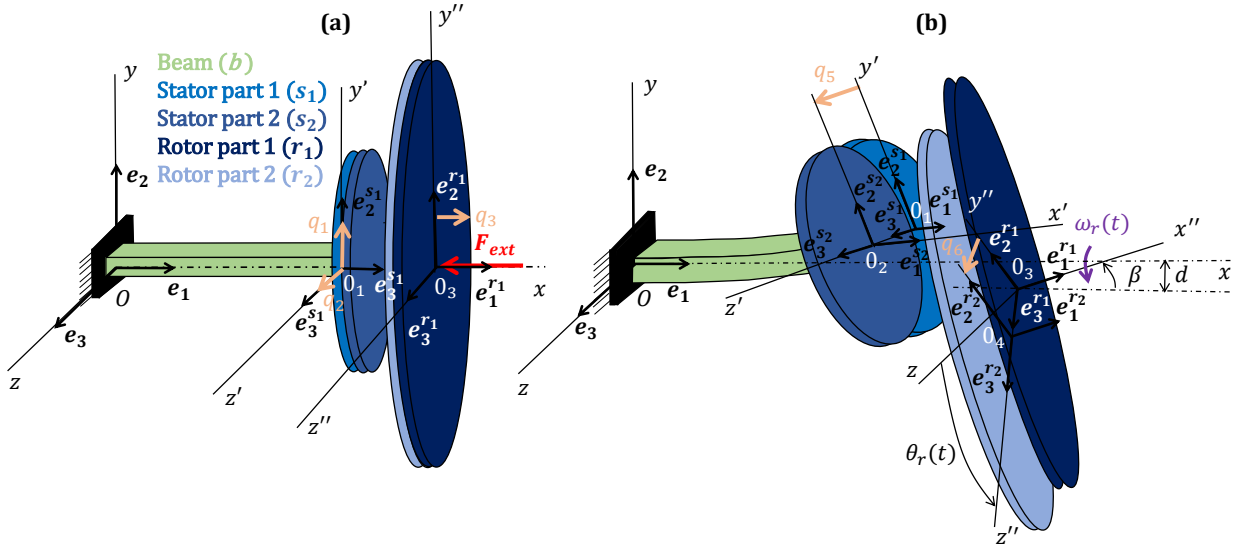

Figure 1: Presentation of the phenomenological model. (a) Different parts of the associated mechanical system. (b) System movement with inclination angle β and center distance d_1.

3. Motion equations

The kinetic and potential energies of the beam are written in the first, as presented in Annex 1. Then, the generalized force containing a contact and friction stress at the interface $(s_2 - r_2)$ is expressed and the developement is presented in Annex 2. Finally, the use of *Lagrange* equations gives rise to the discrete problem containing a system of second-order nonlinear differential equations, stated as follows:

Find $\boldsymbol{q} : \mathbb{T} \longrightarrow \mathbb{R}^5$ such that:

$$\forall t \in \mathbb{T}, \begin{cases} \dfrac{\mathrm{d}}{\mathrm{dt}}\left(\dfrac{\partial \mathcal{L}}{\partial \dot{\boldsymbol{q}}(t)}\right) - \dfrac{\partial \mathcal{L}}{\partial \boldsymbol{q}(t)} = \boldsymbol{Q}(t) & (\textit{Lagrange} \text{ equations}) \\ \boldsymbol{q}(0) = \boldsymbol{q_0} & (\text{Displacements initial condition}) \\ \dot{\boldsymbol{q}}(0) = \dot{\boldsymbol{q}}_{\boldsymbol{0}} & (\text{Velocities initial condition}) \end{cases} \tag{6}$$

with:

- $\boldsymbol{q}(t) = \begin{bmatrix} q_1(t) & q_2(t) & q_3(t) & q_5(t) & q_6(t) \end{bmatrix}^T \in \mathbb{R}^5$ (respectively $\dot{\boldsymbol{q}}(t) = \begin{bmatrix} \dot{q}_1(t) & \dot{q}_2(t) & \dot{q}_3(t) & \dot{q}_5(t) & \dot{q}_6(t) \end{bmatrix}^T \in \mathbb{R}^5$), the vector containing the generalized coordinates (respectively the temporal derivative of generalized coordinates).
- $\mathcal{L} : \mathbb{R}^5 \times \mathbb{R}^5 \times \mathbb{T} \longrightarrow \mathbb{R}$, $(\boldsymbol{q}(t), \dot{\boldsymbol{q}}(t), t) \longmapsto \mathcal{L}(\boldsymbol{q}(t), \dot{\boldsymbol{q}}(t), t) = \mathcal{T}^{\mathcal{S}}_{/R_0}(t) - \mathcal{V}^{\mathcal{S}}_{/R_0}(t)$, is the Lagrangien. Here, $\mathcal{T}^{\mathcal{S}}_{/R_0}(t) = \mathcal{T}^{b}_{/R_0}(t) + \mathcal{T}_{/}$ is the sum of all kinetic energies and $\mathcal{V}^{\mathcal{S}}_{/R_0}(t) = \mathcal{V}^{b}_{/R_0}(t)$ is the sum of all potential energies given in Annex 1.
- $\boldsymbol{Q}(t) = \boldsymbol{Q^{s_2}}(t) + \boldsymbol{Q^{r_2}}(t) + \boldsymbol{Q^{s_1}}(t) + \boldsymbol{Q^{r_1}}(t) \in \mathbb{R}^5$, the vector including the generalized forces at interfaces $(s_2 - r_2)$, $(s_1 - s_2)$ and $(r_1 - r_2)$ given in Annex 2.

The nonlinear differential equations system of the problem (6) can be written matricially:

Find $\boldsymbol{q} : \mathbb{T} \longrightarrow \mathbb{R}^5$ such that:

$$\forall t \in \mathbb{T}, \begin{cases} \boldsymbol{M}\,\ddot{\boldsymbol{q}}(t) + \boldsymbol{K}\,\boldsymbol{q}(t) = \boldsymbol{Q}\,(t) & (\text{Second order differential equations system}) \\ \boldsymbol{q}(0) = \boldsymbol{q_0} & (\text{Displacements initial condition}) \\ \dot{\boldsymbol{q}}(0) = \dot{\boldsymbol{q}}_{\boldsymbol{0}} & (\text{Velocities initial condition}) \end{cases} \tag{7}$$

with:

- $\boldsymbol{M} \in \mathcal{M}_{5,5}(\mathbb{R})$, the mass matrix.
- $\mathbf{K} \in \mathcal{M}_{5,5}(\mathbb{R})$, the stiffness matrix.

In order to be able to work more efficiently, the system of second-order nonlinear differential equations of dimension 4 (7) is put in the state form. This gives rise to the following problem containing a nonlinear differential inclusions system of the first order:

Find $\boldsymbol{X} : \mathbb{T} \longrightarrow X \subset \mathbb{R}^{10}$ such that:

$$\forall t \in \mathbb{T}, \begin{cases} \dot{\boldsymbol{X}}(t) = \boldsymbol{G}(\boldsymbol{X}(t), t) \\ \boldsymbol{X}(0) = \boldsymbol{X_0} \end{cases} \tag{8}$$

with:

- $\boldsymbol{X}(t) = \begin{bmatrix} \boldsymbol{q}(t) \\ \dot{\boldsymbol{q}}(t) \end{bmatrix} \in X \subset \mathbb{R}^{10}$, the state vector composed of generalized coordinates as well as their temporal variations.
- $\boldsymbol{G_L} : X \longrightarrow \mathbb{R}^{10}, (\boldsymbol{X}(t)) \mapsto \boldsymbol{L}\boldsymbol{X}(t)$, a linear map having the associated matrix $\boldsymbol{L}\left(\boldsymbol{G_L} \in \mathcal{L}\left(X, \mathbb{R}^{10}\right)\right)$.
- $\boldsymbol{L} = \begin{bmatrix} \mathbf{0} & \boldsymbol{I} \\ -\boldsymbol{M}^{-1}\boldsymbol{K} & \mathbf{0} \end{bmatrix} \in \mathcal{M}_{10,10}(\mathbb{R})$, the matrix associated with the linear map $\boldsymbol{G_L}$.
- $\boldsymbol{G} : X \times \mathbb{T} \longrightarrow \mathbb{R}^{10}$, a nonlinear application.

At the end, the knowledge at each instant $t \in \mathbb{T}$ of the state of the mechanical system contained in vector $\boldsymbol{X}(t)$ is derived by means of a temporal integration of the system of differential equations (8). Mathematically, it is a non-autonomous dynamic system named $\mathcal{S}^{pheno} = \left(X \subset \mathbb{R}^{10}, \mathbb{T}, \boldsymbol{\varphi}_{\boldsymbol{t}}^{\boldsymbol{pheno}}\right)$. $\boldsymbol{\varphi^{pheno}} : X \times \mathbb{T} \longrightarrow \mathbb{R}^{10}$ is the flow defined implicitly by the system of differential equations (8).

4. Parametric study

The main idea of this paper is to study the influence of goemetrical three imperfections (gap in the link associated with $q_5(t)$ and $q_6(t)$, center distance d, inclination angle β) on the stability and the dynamical behavior of mechanical systems using a phenomenological model. After presenting the equations describing the dynamics of the phenomenological model, a parametric study is carried out, divided into two parts. This division into two parts is due to the requirement to take into account a radial gap at interface $(r_1 - r_2)$. Indeed, the rotation of the rotor disc induces friction on the area of interface $(s_2 - r_2)$ in contact. In addition, inclination angle β of rotor disc r accentuates the non-homogeneous pressure distribution at this interface. Consequently, when a gap exists at interface $(r_1 - r_2)$, these two phenomena (friction and pressure distribution) naturally induce a periodic relative sliding of rotor disc r_2 relative to r_1. This periodicity is related to the rotation of rotor disc r. On the other hand, if there is no gap (link $(r_1 - r_2)$ blocked), these periodic relative slidings are not possible. If a gap exists in link $(s_1 - s_2)$, a relative sliding also appears and is periodic only if link $(r_1 - r_2)$ is unblocked. These geometric imperfections and in particular the gap in the connection $(r_1 - r_2)$ and the inclination β of the rotating part are not often taken into account in current models. Without these imperfections, the angular position $\theta_4(t)$ changes nothing and the physical phenomena are invariant. This is why, very often, the rotation does not appear in the equations and is often not taken into account or even forgotten. Only the rotation velocity should appear since it has an important influence on the stability and on the dynamic behavior, as shown in [40]. It should be understood that rotation $\theta_4(t)$ is important when these imperfections are present, which is always the case in practice. This is why the aim of these two parts is to demonstrate the importance of taking into account these geometric imperfections in the modeling of mechanical systems whose design can be linked to the phenomenological model presented.

The first part of this study contains **cases 1** and **2** described in table (2) and for which link $(r_1 - r_2)$ is always blocked $(q_6(t) = 0, \forall t \in \mathbb{T})$. Consequently, rotation angle $\theta_r(t)$, $t \in \mathbb{T}$ of rotor disc r_1 does not appear in the equations (8) (vectors field $\boldsymbol{G}$), which implies that the dynamic system $\mathcal{S}^{pheno}$ is autonomous. In order to study these two first cases, the methods associated with fixed point calculus and the associated stability analysis can be used. Indeed, and given that the dynamic system $\mathcal{S}^{pheno}$ is autonomous, for each parameter set $k \in \mathcal{I}_p$, there exists an associated fixed point denoted $\boldsymbol{X}_e^k$. In **case 1**, link $(s_1 - s_2)$ is blocked and the associated stiffness k_1 tends to infinity. In **case 2** the opposite is true: link $(s_1 - s_2)$ is unblocked and a nonlinear stiffness $k_1(q_5(t))$ described in Annex B is used and allows one to take into account a certain gap, contacts (stop) and friction in the sliding link. The status of link $(s_1 - s_2)$ has no influence on the dynamic system $\mathcal{S}^{pheno}$. Indeed, the system remains autonomous even if the slide link $(s_1 - s_2)$ is unblocked.

The second part of this study consists of **cases 3** and **4**, also described in table (2), for which the slide link $(r_1 - r_2)$ is unblocked $(q_6(t) \neq 0, \forall t \in \mathbb{T})$. Consequently, the dynamic system $\mathcal{S}^{pheno}$ is no longer autonomous because of the presence of rotation angle $\theta_r(t)$ in the equations. This implies that a fixed point no longer exists for each parameter set $k \in \mathcal{I}_p$. In fact, it is a forced dynamic system where $T_r = \frac{\omega_r}{2\pi}$ is the period of excitation associated with rotor rotation $\theta_r(t)$. Methods including calculations of the periodic orbitals as well as their stability (construction of the Monodromy matrix) must be used in the second part of this parametric study. As in the first part, in **case 3**, the slide link $(r_1 - r_2)$ is blocked and the associated stiffness k_2 tends to infinity. In **case 4** the opposite is true, link $(r_1 - r_2)$ is unblocked and a nonlinear stiffness $k_2(q_6(t))$ described in Annex B is used and allows one to take into account a certain gap, contacts (stop) and friction in the sliding link .

Generally, only three parameters are studied: the friction coefficient at interface $(s_2 - r_2)$, rotation angle β and center distance d. Rotation velocity ω_r is fixed at 100 rad/s and exterior force F_{ext} at 2000 N.

Case	k_1 [N/m^3] (q_5 [m])	k_2 [N/m^3] (q_6 [m])	$\mu_{s_2-r_2}$	ω_r [rad/s]	β [°]	d[m]	F_{ext} [N]
1	$+\infty$ (0)	$+\infty$ (0)	[0, 1]	100	{0;1;1.75}	{0;5;10}.10^{-3}	2000
2	$k_1(q_5(t))$	$+\infty$ (0)	[0, 1]	100	{0;1;1.75}	{0;5;10}.10^{-3}	2000
3	$k_1(q_5(t))$	$k_2(q_6(t))$	[0, 1]	100	{0;1;1.75}	{0;5;10}.10^{-3}	2000
4	$+\infty$ (0)	$k_2(q_6(t))$	[0, 1]	100	{0;1;1.75}	{0;5;10}.10^{-3}	2000

Table 2: Different **cases** tested from **1** to **4**

*4.1. Automous dynamical system (**cases 1** and **2**)*

In this first part of this study, link $(r_1 - r_2)$ is blocked. Mathematically, this implies that the dynamic system $\mathcal{S}^{pheno} = \left(X \subset \mathbb{R}^5, \mathbb{T}, \boldsymbol{\varphi}_t^{\boldsymbol{pheno}}\right)$ is autonomous. In fact, time t and, more precisely, $\omega_r\, t$, does not appear explicitly in the vector field $\boldsymbol{G}$. It is thus possible to find, for each set of variable parameters $\boldsymbol{W}^k \in \mathbb{R}^3$, $k \in \mathcal{I}_p$, an associated fixed point denoted $\boldsymbol{X}_e^k$. This is a sliding static equilibrium state, as the rotor disc r_1 is always considered in rotation and there is always friction at interface $(s_2 - r_2)$. For a dynamic system whose flow $\boldsymbol{\varphi}^{\boldsymbol{pheno}}$ is implicitly defined by a system of nonlinear differential equations, this consists of writing for each set of parameters:

$$\forall k \in \mathcal{I}_p, \quad \dot{\boldsymbol{X}}_{\boldsymbol{e}}^{\boldsymbol{k}} = \boldsymbol{0} \iff \boldsymbol{G}(\boldsymbol{X}_{\boldsymbol{e}}^{\boldsymbol{k}}, \boldsymbol{W}^{\boldsymbol{k}}) = \boldsymbol{0} \tag{9}$$

Using the *Newton-Raphson* method, it is possible to construct a sequence $\left(\boldsymbol{Y}_{\boldsymbol{i}}^{\boldsymbol{k}}\right)_{i\in\mathbb{N}} (\boldsymbol{Y}_{\boldsymbol{i}}^{\boldsymbol{k}} \underset{i\to\infty}{\longrightarrow} \boldsymbol{X}_{\boldsymbol{e}}^{\boldsymbol{k}})$ for each set of parameters $k \in \mathcal{I}_p$. This sequence is defined by the following recurrence relation:

$$\forall k \in \mathcal{I}_p,\ \forall\, i \in \mathbb{N}, \begin{cases} \boldsymbol{Y}_{\boldsymbol{i+1}}^{\boldsymbol{k}} = \boldsymbol{Y}_{\boldsymbol{i}}^{\boldsymbol{k}} + \left(\boldsymbol{J}\left(\boldsymbol{G}(\boldsymbol{Y}_{\boldsymbol{i}}^{\boldsymbol{k}}), \boldsymbol{W}^{\boldsymbol{k}}\right)\right)^{-1} \boldsymbol{G}(\boldsymbol{Y}_{\boldsymbol{i}}^{\boldsymbol{k}}, \boldsymbol{W}^{\boldsymbol{k}}) \\ \sigma_{n,i}^k(\boldsymbol{x}, t) = \rho_c\, \Delta u_{n,i}^k(\boldsymbol{x}, t) \quad \forall \boldsymbol{x} \in \Gamma_{s_2}^{cf}(t) \\ \boldsymbol{\sigma}_{\boldsymbol{t,i}}^{\boldsymbol{k}}(\boldsymbol{x}, t) = \mu_{s_2 - r_2}\, \sigma_{n,i}^k(\boldsymbol{x}, t)\, \boldsymbol{e}_{\boldsymbol{t}}^{\boldsymbol{cf}}(\boldsymbol{x}, t) \quad \forall \boldsymbol{x} \in \Gamma_{s_2}^{cf}(t) \end{cases} \tag{10}$$

The stability of each fixed point $\boldsymbol{X}_{\boldsymbol{e}}^{\boldsymbol{k}}$, $\forall k \in \mathcal{I}_p$, is achieved by building the Jacobian matrix denoted $\boldsymbol{A}^{\boldsymbol{k}}$ coming from the limited development to the first order of the vector field $\boldsymbol{G}$ around the fixed point $\boldsymbol{X}_{\boldsymbol{e}}^{\boldsymbol{k}}$. By using the finite difference method, the Jacobian matrix is approximated for each set of parameters, $k \in \mathcal{I}_p$, as follows:

$$\tilde{\boldsymbol{A}}^{\boldsymbol{k}} = \frac{\boldsymbol{G}\left(\boldsymbol{X}_{\boldsymbol{e}}^{\boldsymbol{k}}, \boldsymbol{W}^{\boldsymbol{k}} + \delta \boldsymbol{X}_{\boldsymbol{e}}^{\boldsymbol{k}}\right) - \boldsymbol{G}\left(\boldsymbol{X}_{\boldsymbol{e}}^{\boldsymbol{k}}, \boldsymbol{W}^{\boldsymbol{k}}\right)}{\delta \boldsymbol{X}_{\boldsymbol{e}}^{\boldsymbol{k}}}, \quad \delta \boldsymbol{X}_{\boldsymbol{e}}^{\boldsymbol{k}} \longrightarrow \boldsymbol{0} \ \ \forall k \in \mathcal{I}_p \tag{11}$$

Then, in order to find out the behavior of the system and in particular the vibratory amplitudes, temporal integrations of the differential equations system from many fixed point must be carried out. For this, a discretization of set $\mathbb{T}$ into N equal parts of length $h \in \mathbb{R}$ allows the construction of a sequence $\left(\tilde{\boldsymbol{t}}_{\boldsymbol{n}}\right)_{n\in\mathcal{I}_t}$, $\mathcal{I}_t = \{0; 2; \cdots; N\} \subset \mathbb{N}$. Finally, the integrations are carried out with the *Runge-Kutta* 4 scheme. This allows the construction of a second sequence denoted $\left(\tilde{\boldsymbol{X}}_{\boldsymbol{n}}\right)_{n\in\mathcal{I}_t}$ (where $\tilde{\boldsymbol{X}}_{\boldsymbol{n}} \simeq \boldsymbol{X}(t_n)$) whose recurrence relation is as follows:

$$\tilde{\boldsymbol{X}}_{\boldsymbol{n+1}} = \boldsymbol{H}^{\boldsymbol{RK_4}}(\tilde{\boldsymbol{X}}_{\boldsymbol{n}}, n) \quad \forall n \in \mathcal{I}_t \tag{12}$$

with:

- $\boldsymbol{H}^{\boldsymbol{RK_4}} : X \times \mathcal{I}_t \longrightarrow \mathbb{R}^{10}, (\tilde{\boldsymbol{X}}_{\boldsymbol{n}}, n) \longmapsto \tilde{\boldsymbol{X}}_{\boldsymbol{n}} + \dfrac{\Delta t}{6}\,(\boldsymbol{k_1} + 2\,\boldsymbol{k_2} + 2\,\boldsymbol{k_3} + \boldsymbol{k_4}) \simeq \tilde{\boldsymbol{X}}_{\boldsymbol{n}} + \displaystyle\int_{t_n}^{t_{n+1}} \boldsymbol{G}(\tilde{\boldsymbol{X}}_{\boldsymbol{n}}, t_n)\, dt$, the *Runge-Kutta* 4 application where $\Delta t = t_{n+1} - t_n$ is the time step coming from of recurrence relation associated with the sequence $\left(\tilde{\boldsymbol{t}}_{\boldsymbol{n}}\right)_{n\in\mathcal{I}_t}$.
- $\boldsymbol{k_1} = \boldsymbol{G}(\tilde{\boldsymbol{X}}_{\boldsymbol{n}}, t_n)$, the slope at the start of the interval.
- $\boldsymbol{k_2} = \boldsymbol{G}(\tilde{\boldsymbol{X}}_{\boldsymbol{n}} + \dfrac{\Delta t}{2}\,\boldsymbol{k_1}, t_n + \dfrac{\Delta t}{2})$, the slope in the middle of the interval obtained with $\boldsymbol{k_1}$.
- $\boldsymbol{k_3} = \boldsymbol{G}(\tilde{\boldsymbol{X}}_{\boldsymbol{n}} + \dfrac{\Delta t}{2}\,\boldsymbol{k_2}, t_n + \dfrac{\Delta t}{2})$, the slope in the middle of the interval obtained with $\boldsymbol{k_2}$.
- $\boldsymbol{k_4} = \boldsymbol{G}(\tilde{\boldsymbol{X}}_{\boldsymbol{n}} + \Delta t\,\boldsymbol{k_3}, t_n + \Delta t)$, the slope at the end of the interval.

In this first case, the locking of the displacement of stator s_2 following the direction z' corresponds to the null gap at interface $(s_1 - s_2)$. The parametric study associated with this first case is greatly simplified. Indeed, it consists in the first place in determining the fixed point associated with each set of parameters k, $k \in \mathcal{I}_p$. Then the stability of each

fixed point is studied. Finally, temporal integrations initiated from the calculated fixed points are carried out.
The first influence studied is associated with parameter d corresponding to the center distance following direction y between rotor disc r_1 and stator disc s_1. In a first phase, the fixed points of the dynamical system $\mathcal{S}^{pheno}$ are determined for each parameter set $k \in \mathcal{I}_p$. Figure (2) shows the evolutions of each component of fixed point $\boldsymbol{X_e}$ with respect to friction coefficient $\mu_{s_2-r_2}$, for a force $F_{ext} = 2000$ N, a rotor velocity rotation $\omega_r = 100$ rad/s and three values of the center distance d (0, 5.10^{-3} and 5.10^{-3} m). Generally, the increase in the center distance parameter d induces an increase in the bending at the end of the beam (point O_1) following direction z, as shown by the generalized coordinates q_2^{eq}. For the bending following direction y (generalized coordinate q_1^{eq}), the behavior is the same until friction coeffcient $\mu_{s_2-r_2}$ reaches 0.5, then the bending decreases. The associated levels remain low (maximum $5\,10^{-6}$ m), which allows one to conclude that the center distance parameters have very little influence on the fixed point of the dynamic system $\mathcal{S}^{pheno}$. Next, it is the stability of the fixed points calculated previously which is analyzed. Figure (3) shows the evolution of real part $Re(\lambda)$ (a) and eigenfrequency $f = \frac{Im(\lambda)}{2\pi}$ (b) with respect to friction coefficient $\mu_{s_2-r_2}$ at interface $(s_2 - r_2)$ for an exterior force $F_{ext} = 2000$ N, a rotor velocity rotation $\omega_r = 100$ rad/s and for three angles β (0, 1 and 1.75 °). For an angle $\beta = 0$, the real part of each eigenvalue λ is null before the bifurcation point (black point in figure (3 (a)). This is a *Hopf* bifurcation of fixed point and of codimension 1. Indeed, only the variation in friction coefficient $\mu_{s_2-r_2}$ allows this bifurcation. It corresponds to the coalescence of two bending modes of the beam following directions y and z, as observed in figure 3 (b). The center distance d has very little influence on the value of friction coefficient $\mu_{s_2-r_2}$ allowing the bifurcation. In the third phase, temporal integrations are realized with the *Runge-Kutta* 4 scheme from three fixed points, as represented in figure (4). The center distance also has very little influence on the dynamic behavior, especially the levels of limit cycles. This non-influence of the center distance on the stability and the dynamics initially stems from the value of the parameter d, which must be realistic. Moreover, with these values of d, the tangential stress field $\boldsymbol{\sigma_t}$ at the interface $(s_2 - r_2)$, changes little.
The second influence is studied with parameter β, corresponding to the inclination angle of rotor disc r_1 around direction z. As previously, calculations of fixed points, a stability analysis of these fixed points and temporal integrations are done. Figures (5) and (6) show the same evolutions as previously, but for three values of angle β: 0, 1 and 1.75 °. For $\beta = 0$, the bifurcation point is the same as previously. Neverthless, with higher values of β (1 and 1.75 °), changes in fixed points are significant and the *Hopf* bifurcation appears for higher values of $\mu_{s_2-r_2}$ (about $\mu_{s_2-r_2} = 0.2$ for $\beta = 1$ and $\mu_{s_2-r_2} = 0.4$ for $\beta = 1.75$). Moreover, the coalescence of frequencies (bending mode of the beam) observed with $\beta = 0$ no longer appears for an inclination angle β different from zero; however whirl instability is always present. The decrease of the eigenfrequencies is due to the inclination angle β of the rotor disc r_1 other than zero which generates a more or less large separation on an associated part of the interface $(s_2 - r_2)$. Consequently, the overall normal force decreases, which induces a decrease of the generalized forces $Q_1(t)$ and $Q_2(t)$. By carrying out the limited development of these two forces generalized around each fixed point $\boldsymbol{X_e^k}$ (corresponding to each coefficient of friction $\mu_{s_2-r_2}$) at the first order, the coefficients (corresponding to stiffness) of the monomials associated with the generalized coordinates $q_1(t)$ and $q_2(t)$, are weaker than in the case where $\beta = 0$. This reduction has a direct impact on the eigenfrequencies. Concerning the loss of coalescence of the proper frequencies, this is due to the gyroscopic terms corresponding to those of the monomials associated with the generalized coordinates $\dot{q}_1(t)$ and $\dot{q}_2(t)$. In conclusion, the decrease in eigenfrequencies with the inclination angle β and the loss of coalescence demonstrate the importance of taking this geometric imperfection into account in the model. In figure (7), the temporal integrations initiated from three fixed points are presented for a friction coefficient $\mu_{s_2-r_2} = 0.4$. An influence of the inclination angle β on the levels of the limit cycles can be observed. In fact, the maximum amplitude of the limit cycle decreases when angle β increases, as observed for angles $\beta = 0$ and $\beta = 1$ in figure (7). This is due to the inclination which increases the pressure (normal stress $\sigma_n(\boldsymbol{x}, t)$) at each point of the part of the interface $\bar{\Gamma}_{s_2}^{cf}(t)$ in contact with the rotor disc r_2 and consequently the friction stress $\sigma_t(\boldsymbol{x}, t)$. Finally, in the first order, a damping appears as shown in figure (6) and increases with the angle of inclination β. In addition, this friction has the effect of limiting the levels as shown in figure (7).

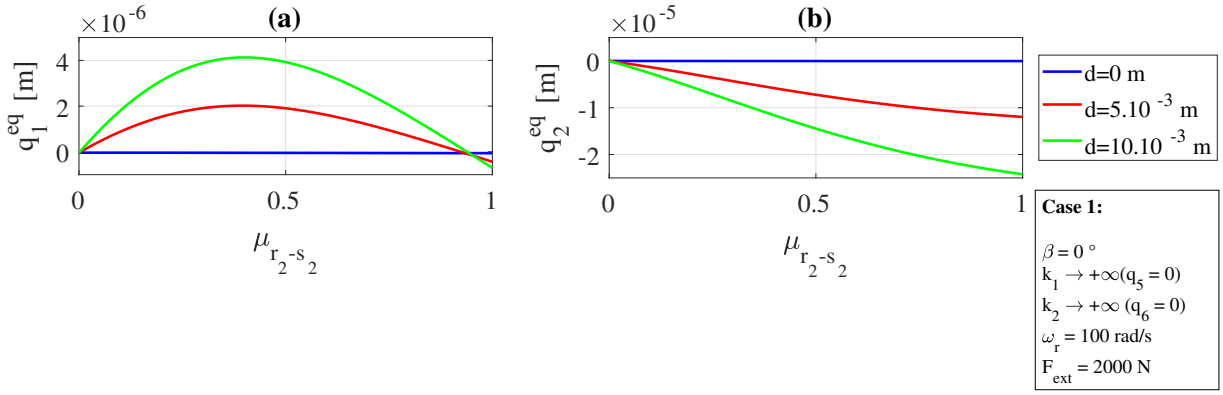

Figure 2: Evolution of fixed points $\boldsymbol{X_e}$ of dynamical system $\mathcal{S}^{pheno}$ with respect to friction coefficient $\mu_{s_2-r_2}$ for **case 1** ($k_1 \rightarrow +\infty$, $k_2 \rightarrow +\infty$, $\omega_r = 100$ rad/s, $F_{ext} = 2000N$), an angle $\beta = 0$ and 3 values of the center distance d ($d = 0$, 5.10^{-3} and 10.10^{-3} m). (a) Generalized coordinate q_1^{eq}. (b) Generalized coordinate q_2^{eq}.

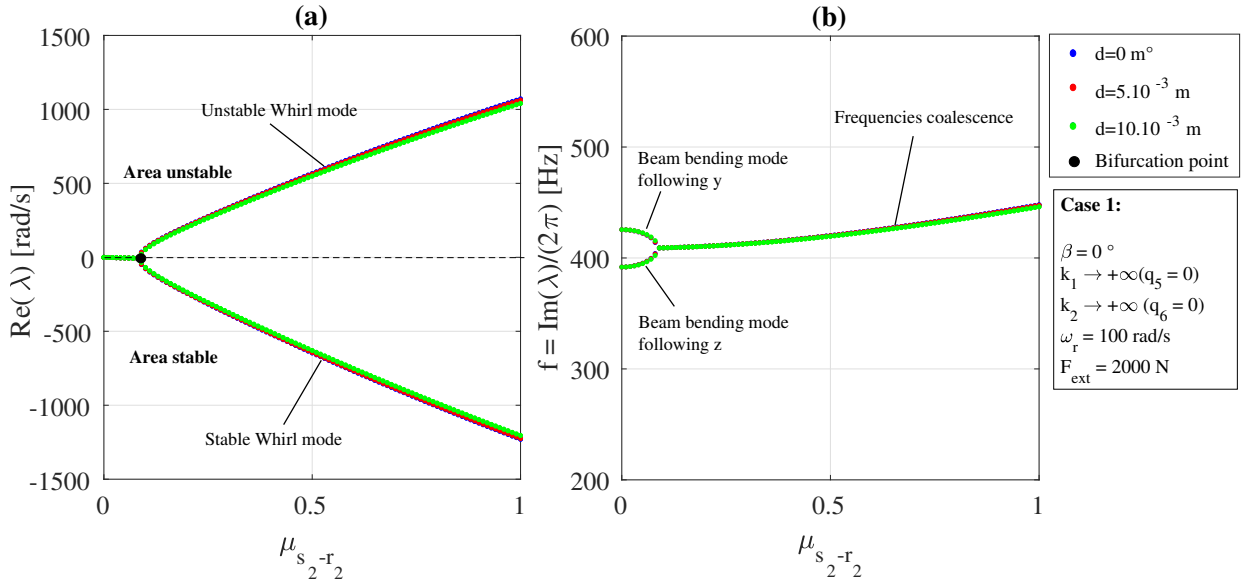

Figure 3: Evolution of eigenvalues λ with respect to friction coefficient $\mu_{s_2-r_2}$ for **case 1** ($k_1 \rightarrow +\infty$, $k_2 \rightarrow +\infty$, $\omega_r = 100$ rad/s, $F_{ext} = 2000N$), an angle $\beta = 0$ and 3 values of the center distance d ($d = 0$, 5.10^{-3} and 10.10^{-3} m). (a) Real part of eigenvalues $Re(\lambda)$. (b) Eigenfrequencies $f = \frac{Im(\lambda)}{2\pi}$.

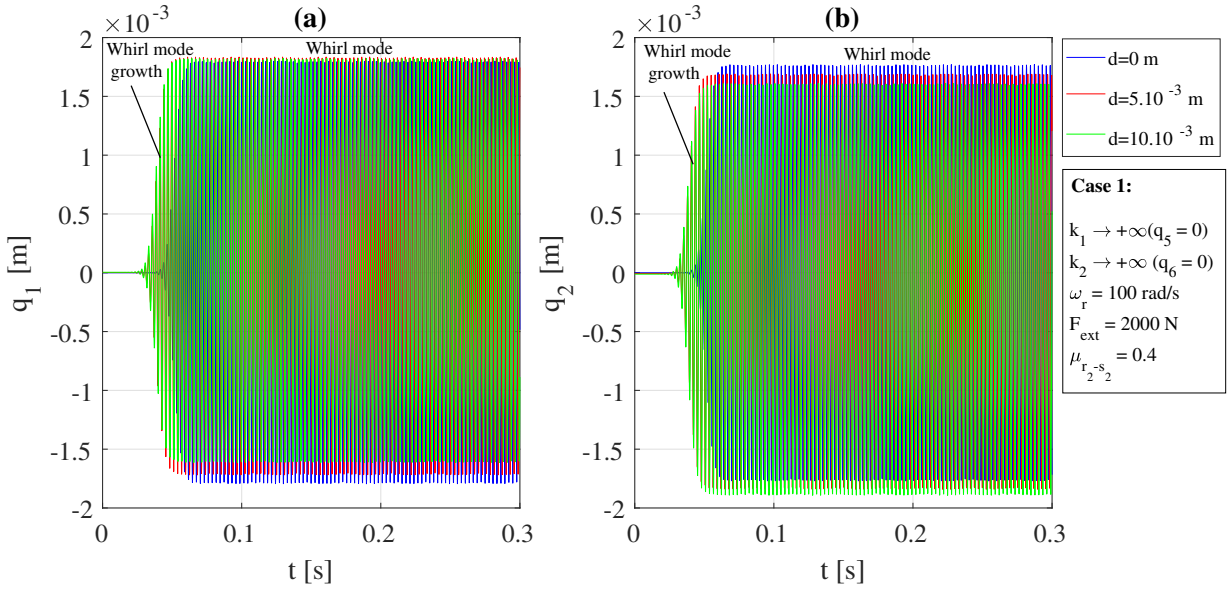

Figure 4: Temporal evolution of the dynamical system state $\boldsymbol{X}$ for **case 1** ($k_1 \to +\infty$, $k_2 \to +\infty$, $\omega_r = 100$ rad/s, $F_{ext} = 2000N$), an angle $\beta = 0$ and 3 values of the center distance d ($d = 0$, 5.10^{-3} and 10.10^{-3} m). (a) Generalized coordinate $q_1(t)$. (b) Generalized coordinate $q_2(t)$.

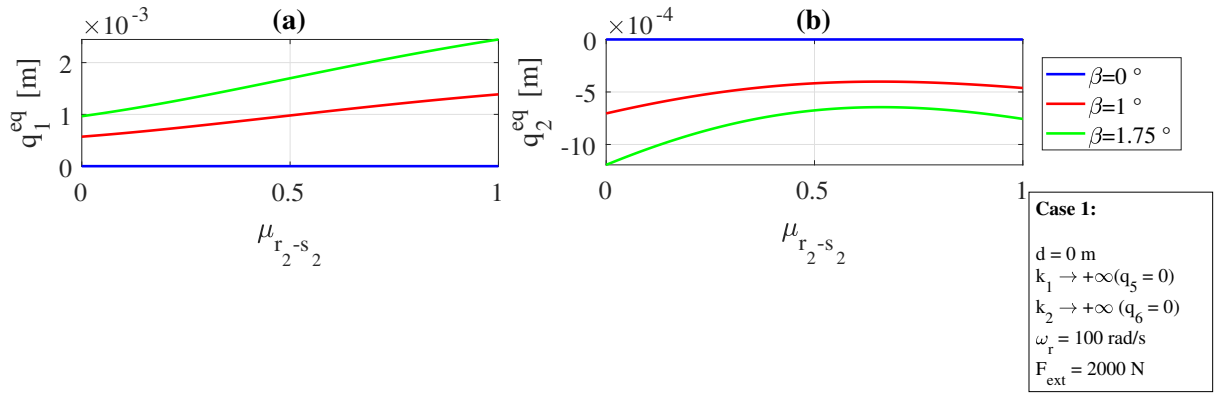

Figure 5: Evolution of fixed points $\boldsymbol{X_e}$ of dynamical system $\mathcal{S}^{pheno}$ with respect to friction coefficient $\mu_{s_2-r_2}$ for **case 1** ($k_1 \to +\infty$, $k_2 \to +\infty$, $\omega_r = 100$ rad/s, $F_{ext} = 2000N$), a center distance $d = 0$ and 3 values of angle β ($\beta = 0$, 1 and 1.75 °). (a) Generalized coordinate q_1^{eq}. (b) Generalized coordinate q_2^{eq}.

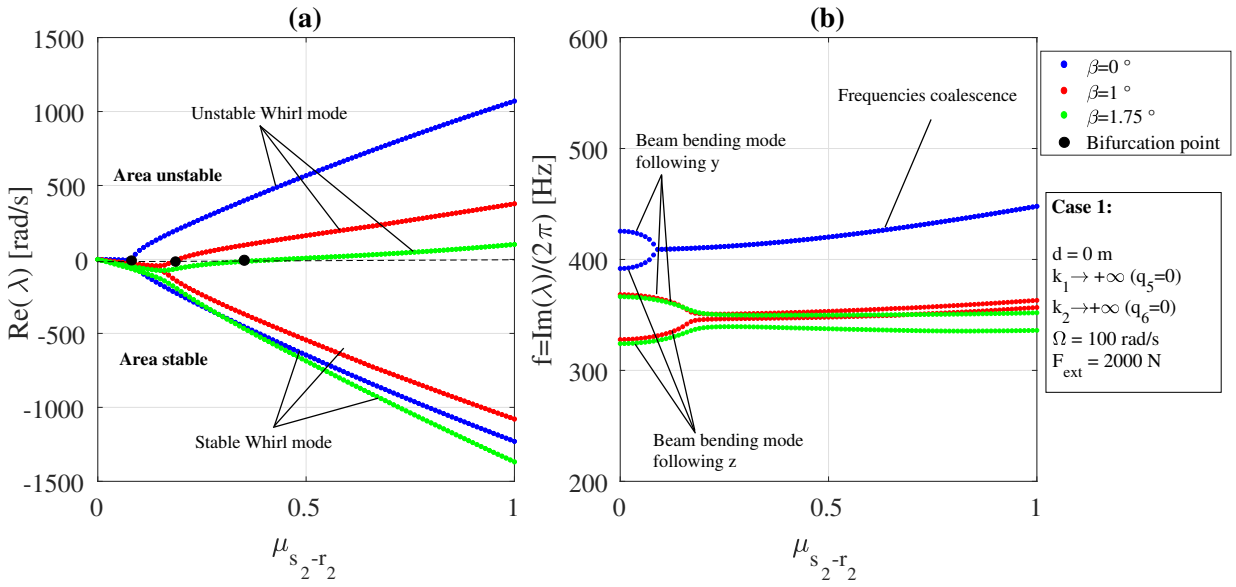

Figure 6: Evolution of eigenvalues λ with respect to friction coefficient $\mu_{s_2-r_2}$ for **case 1** ($k_1 \to +\infty$, $k_2 \to +\infty$, $\omega_r = 100$ rad/s, $F_{ext} = 2000N$), a center distance $d = 0$ and 3 values of the angle β ($\beta = 0$, 1 and 1.75 °). (a) Real part of eigenvalues $Re(\lambda)$. (b) Eigenfrequencies $f = \frac{Im(\lambda)}{2\pi}$.

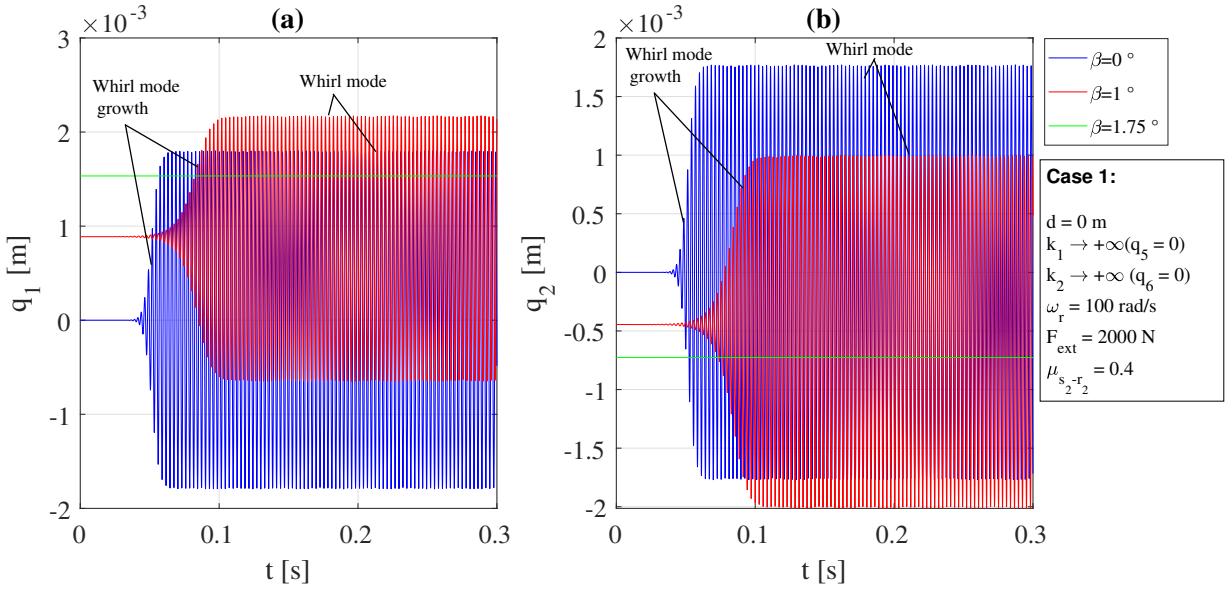

Figure 7: Temporal evolution of the dynamical system state $\boldsymbol{X}$ for **case 1** ($k_1 \to +\infty$, $k_2 \to +\infty$, $\omega_r = 100$ rad/s, $F_{ext} = 2000N$), a center distance $d = 0$ and 3 values of angle β ($\beta = 0$, 1 and 1.75 °). (a) Generalized coordinate $q_1(t)$. (b) Generalized coordinate $q_2(t)$.

In this second case, link $(s_1 - s_2)$ is unblocked and the value of the linear part of stiffness k_1 is fixed at 2.10^6 N/m. As explained previously, this is a simplification of the modeling of the phenomena at interface $(s_1 - s_2)$ which accounts for both contact and friction in direction y'. Moreover and for the reasons mentioned previously, blocking link $(r_1 - r_2)$ $(q_6(t) = 0)$ simplifies the vector's field expression $\boldsymbol{G}$.

In the first phase, the fixed points are determined for each value of inclination angle β (0, 1 and 1.75 °). The values of

the other parameters are the same as in **case 1**, namely $F_{ext} = 2000$ and $\omega_r = 100$ rad/s. The fixed points are plotted in figure (8) with respect to friction coefficient $\mu_{s_2-r_2}$. For the generalized coordinates q_1^{eq} and q_2^{eq}, there is no difference with **case 1**, namely the increase of the amplitude when the coefficient of friction increases. For q_5^{eq}, the observation is the same as for q_1^{eq} and q_2^{eq}. This is normal because there is gap j_1 in the link $(s_1 - s_2)$ and therefore the disc stator s_2 can move relatively to s_1. In the second phase, the stability of each fixed point is studied. The evolutions of the real and imaginary parts (eigenfrequencies $f = \frac{Im(\lambda)}{2\pi}$) of the eigenvalues with respect to friction coefficient $\mu_{s_2-r_2}$ at interface $(s_2 - r_2)$ are plotted in figure (9). The first observation is a shift of the bifurcation point compared to **case 1**. Indeed, for $\beta = 0$, the value of $\mu_{s_2-r_2}$ inducing a *Hopf* bifurcation is about 0.3. This value is about 0.1 when $k_1 \to +\infty$ $(q_5(t) = 0\ ,t \in \mathbb{T})$ (**case 1**). For the other values, the observation is the same, and for $\beta = 1.75$, there is no bifurcation point before $\mu_{s_2-r_2} = 1$. This shift can be explained physically by the sliding of stator disc s_2, limiting the transmission force to beam b and consequently the bending of the latter in direction z. In addition and unlike **case 1**, there is also no coalescence for a zero angle β. As for the inclination, this difference is directly linked to the unblocked link $(s - 1 - s_2)$ which reveals gyroscopic terms (first order monomials in $\dot{q}_1(t)$ and $\dot{q}_2(t)$) despite a zero tilt angle β. Finally, the translation mode of stator disc s_2 is visible in figure (9) and as for the **case 1**, the associated eigenfrequency is higher for an angle β that is null. In the last phase, temporal integrations are performed from the fixed points for a friction coefficient $\mu_{s_2-r_2} = 0.6$ and the evolutions of each generalized coordinate are plotted in figure (10). These evolutions show as for the **case 1**, that the amplitudes of the limit cycles tend to be smaller when inclination angle β increases.

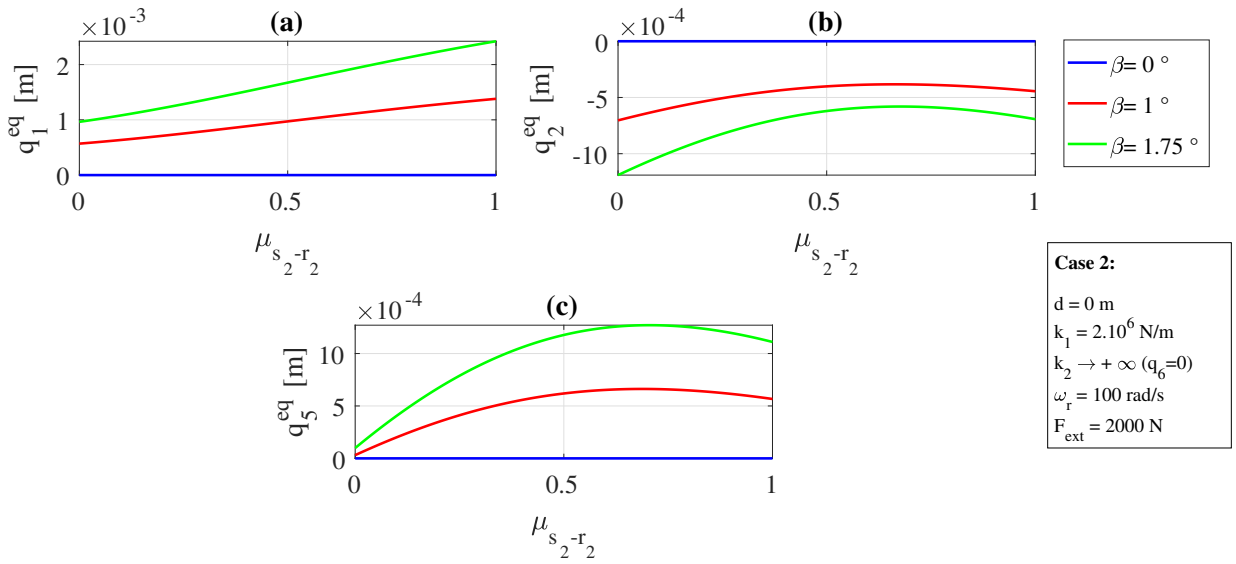

Figure 8: Evolution of fixed points $\boldsymbol{X_e}$ of dynamical system $\mathcal{S}^{pheno}$ with respect to friction coefficient $\mu_{s_2-r_2}$ for **case 2** ($k_1 \to +\infty$, $k_2 \to +\infty$, $\omega_r = 100$ rad/s, $F_{ext} = 2000N$), a center distance $d = 0$ and 3 values of angle β ($\beta = 0$, 1 and 1.75 °). (a) Generalized coordinate q_1^{eq}. (b) Generalized coordinate q_2^{eq}. (c) Generalized coordinate q_5^{eq}.

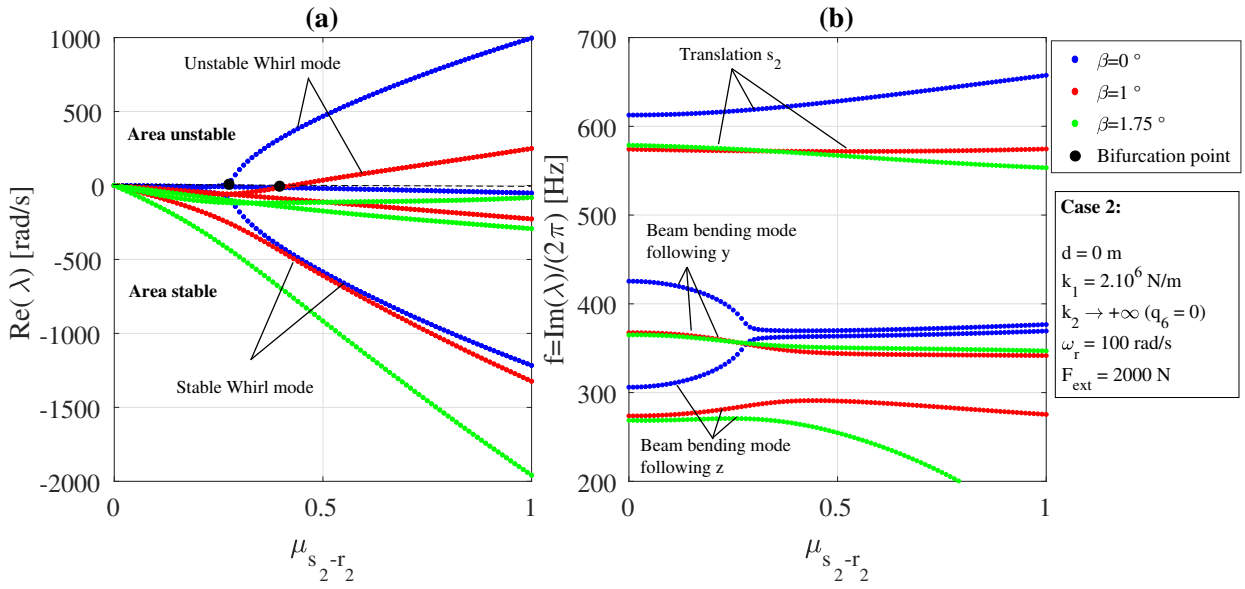

Figure 9: Evolution of eigenvalues λ with respect to friction coefficient $\mu_{s_2-r_2}$ for **case 2** ($k_1 \rightarrow +\infty$, $k_2 \rightarrow +\infty$, ω_r = 100 rad/s, F_{ext} = 2000N), a center distance d = 0 and 3 values of angle β (β = 0, 1 and 1.75 °). (a) Real part of eigenvalues $Re(\lambda)$. (b) Eigenfrequencies $f = \frac{Im(\lambda)}{2\pi}$.

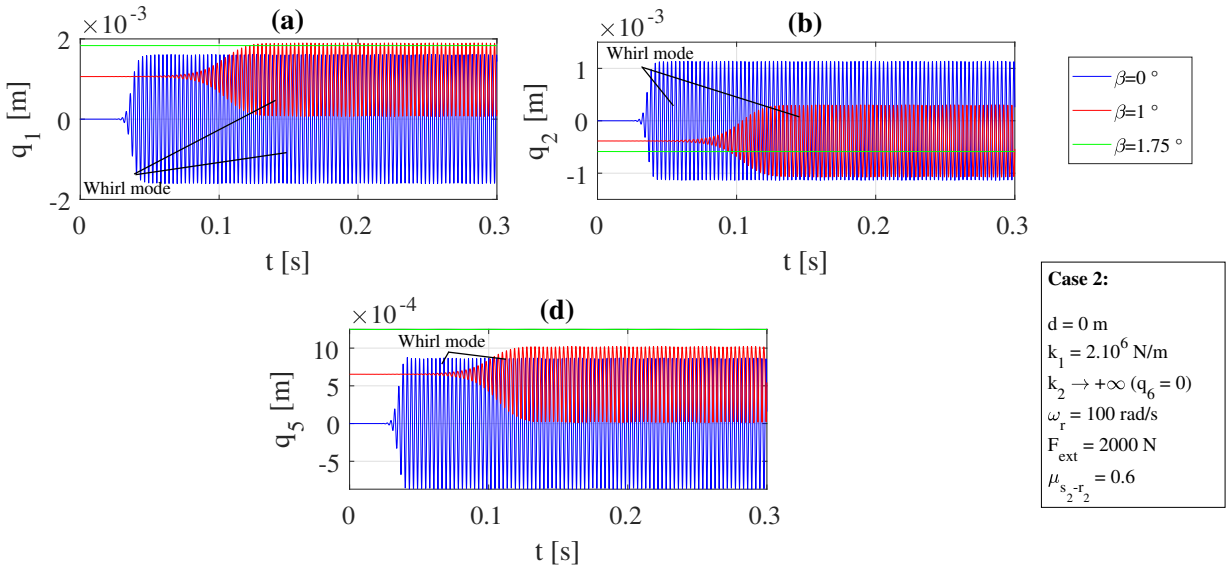

Figure 10: Temporal evolution of the dynamical system state $\boldsymbol{X}$ for **case 2** ($k_1 \rightarrow +\infty$, $k_2 \rightarrow +\infty$, ω_r = 100 rad/s, F_{ext} = 2000N), a center distance d = 0 and 3 values of angle β (β = 0, 1 and 1.75 °). (a) Generalized coordinate $q_1(t)$. (b) Generalized coordinate $q_2(t)$. (c) Generalized coordinate $q_5(t)$.

*4.2. Forced dynamical system (**case 3** and **4**)*

In this second part of the parametric study, link $(r_1 - r_2)$ is unblocked. The existence of a gap j_2 in the link induces new phenomena, as explained previously. The gap in link $(r_1 - r_2)$ coupled with the friction and the rotation of rotor disc r causes a periodic osicllation of the r_2 part of the rotor. To be convinced of this, it is important to note that

inclination angle β of rotor disc r induces a non-homogeneous distribution of the pressure at interface $(s_2 - r_2)$, which is invariant in time $t \in \mathbb{T}$. Moreover, the tangential stress field $\boldsymbol{\sigma_t}$ (friction due to the permanent rotation velocity ω_r) is also invariant in time $t \in \mathbb{T}$. An inclination angle β of rotor disc r around direction z gives rise to a greater pressure on the upper part of interface $(s_2 - r_2)$ than the lower part. A sliding of stator disc s_2 occurs naturally in direction z'. As rotor disc r turns, this slip of s_2 is periodic. For rotor disc r_2, the slip phenomenon also appears but the oscillation period is that of the rotor disc, denoted $T_r = \frac{\omega_r}{2\pi}$, while for s_2, the period is divided by two. The important point to remember is that without the existence of a gap in link $(r_1 - r_2)$, these phenomena of periodic slips cannot appear. In order to confirm these explanations, **cases 3** and **4** are presented and compared to **cases 1** and **2**. Consequently, the dynamic system $\mathcal{S}^{pheno}$ becomes non-autonomous (explicit time dependence) and a periodic excitation takes place. The vector field $\boldsymbol{G}$ thus becomes T_r-periodic. When the system is periodically excited, the determination of fixed points and their associated stability analyses are replaced by calculations of periodic orbits (via temporal integrations) as well as of orbital stability. For the stability, the Monodromy matrix, denoted $\boldsymbol{M_{cycle}}$, associated with each parameter set k, $k \in \mathcal{I}_p$ must be built in the following way:

Let $\boldsymbol{\varphi^{pheno}} : \mathbb{T} \times X \longrightarrow X$, $(t, \boldsymbol{X_0}) \longrightarrow \boldsymbol{\varphi_t^{pheno}}(\boldsymbol{X_0})$, the flow of dynamical system $\mathcal{S}^{pheno} = \left(X, \mathbb{T}, \boldsymbol{\varphi_t^{pheno}}\right)$ implicitly defined by the nonlinear differential equations system given by expression (8). The Monodromy matrix serves to analyze the variations of the solution for a period T following a variation of the initial condition. Therefore, taking $t \longmapsto \boldsymbol{\varphi_t^{pheno}}(\boldsymbol{X_0}^*)$ (respectively $t \longmapsto \boldsymbol{\varphi_t^{pheno}}(\boldsymbol{X_0}^* + \boldsymbol{\delta X_0})$), the periodic solution having as initial condition $\boldsymbol{X_0}^*$ (respectively $\boldsymbol{X_0}^* + \boldsymbol{\delta X_0}$), the temporal evolution of the gap between two solutions is given by:

$$\boldsymbol{\delta X}(t) = \boldsymbol{\varphi_t^{pheno}}(\boldsymbol{X_0}^* + \boldsymbol{\delta X_0}) - \boldsymbol{\varphi_t^{pheno}}(\boldsymbol{X_0}^*),\ \forall t \in \mathbb{T} \tag{13}$$

After a period $T \in \mathbb{T}$ such that $\boldsymbol{X}(t + T) = \boldsymbol{X}(t)$, the gap is written:

$$\boldsymbol{\delta X}(T) = \boldsymbol{\varphi_T^{pheno}}(\boldsymbol{X_0}^* + \boldsymbol{\delta X_0}) - \boldsymbol{\varphi_T^{pheno}}(\boldsymbol{X_0}^*) \tag{14}$$

By performing a limited development at the first order around an initial condition $\boldsymbol{X_0}^*$, we get:

$$\boldsymbol{\delta X}(T) = \frac{\partial \boldsymbol{\varphi_T^{pheno}}(\boldsymbol{X_0}^*)}{\partial \boldsymbol{X_0}} \delta \boldsymbol{X_0} + \mathcal{O}\left(|\delta \boldsymbol{X_0}|^2\right) \tag{15}$$

The set of trajectory variations between two trajectories at $t = T$ is given by the Monodromy matrix $\boldsymbol{M_{cycle}}$, as follows:

$$\boldsymbol{M_{cycle}} = \frac{\partial \boldsymbol{\varphi_T^{pheno}}(\boldsymbol{X_0}^*)}{\partial \boldsymbol{X_0}} \in \mathcal{M}_{10,10}(\mathbb{R}) \tag{16}$$

The spectrum $\mathrm{sp}(\boldsymbol{M_{cycle}})$ of matrix $\boldsymbol{M_{cycle}}$ is obtained by finding the zeros of the characteristic polynomial written as follows:

$$\det(\boldsymbol{M_{cycle}} - \gamma \mathbf{I}) = 0 \tag{17}$$

with:

- $\gamma \in \mathbb{C}$, an eigenvalue of matrix $\boldsymbol{M_{cycle}}$.

In practice, the solution associated with a given initial condition comes from the scheme of *Runge -Kutta* 4. Consequently, it is an approximate solution inducing a dynamic system at a dicrete time denoted $\mathcal{S} = \{X, \mathcal{I}_t, \boldsymbol{\phi_n^{pheno}}\}$ whose flow $\boldsymbol{\phi^{pheno}} : X \times \mathcal{I}_t \longrightarrow \mathbb{R}^{10}, (\boldsymbol{X_0}, t_n) \longmapsto \underbrace{\boldsymbol{H^{RK_4}} \circ \boldsymbol{H^{RK_4}} \cdots \circ \boldsymbol{H^{RK_4}}(\boldsymbol{X_0}, t_n)}_{n \text{ once}}$ comes from the recurrence relation (12). Ultimately, the associated Monodromy matrix is expressed as follows:

$$\tilde{\boldsymbol{M}}_{\boldsymbol{cycle}} = \frac{\partial \boldsymbol{\phi}_{N_c}^{\boldsymbol{pheno}}(\boldsymbol{X_0}^* + \boldsymbol{\delta X_0})}{\partial \boldsymbol{X_0}} \in \mathcal{M}_{10,10}(\mathbb{R}) \tag{18}$$

with:

- $N_c = \min\left(\left\{n \in \mathcal{I}_t \mid \boldsymbol{\phi}^{\boldsymbol{pheno}}_{N_c}(\boldsymbol{X_0}^*) = \boldsymbol{\phi}^{\boldsymbol{pheno}}_{\boldsymbol{0}}(\boldsymbol{X_0}^*)\right\}\right) \in \mathbb{N}$.

Numerically, the previous matrix is determined using the finite difference.

In **case 3**, link $(s_1 - s_2)$ is blocked and $(r_1 - r_2)$ is unblocked. As for the previous cases (**case 1** and **case 2**) and in order to simplify the modeling of the phenomena, a nonlinear stiffness k_2 is used to model the contact with friction at interface $(r_1 - r_2)$. In these two previous cases, rotation angle $\theta_r(t)$ has no influence on the dynamics of the system. Indeed, the blocking of link $(r_1 - r_2)$ induces a simplification of the expression of vector field $\boldsymbol{G}$, removing the terms depending on rotation angle ω_r. Unlike the two previous cases, the calculation of fixed points is no longer possible given the explicit dependence of time $t \in \mathbb{T}$, because of the presence of rotation angle $\theta_r(t)$ in the expression of vector field $\boldsymbol{G}$. It is thus essential to carry out periodic orbital stability studies for each set of parameters $k \in \mathcal{I}_p$. In order to be able to compare the studies and in particular that relating to the stability and the bifurcation point, fixed point calculations and their stability analyses are carried out. This amounts to forcing and considering that rotation angle $\theta_r(t)$ is zero for all of time $t \in \mathbb{T}$. This is an important comparison, given that this rotation angle $\theta_r(t)$ is often overlooked in studies of mechanical systems exhibiting friction-induced vibrations. Indeed, this simplification may be desired in order to simplify the modeling and calculation time. But it can also be unwanted and in this case, important associated phenomena are not modeled.
In a first phase, rotation angle $\theta_r(t)$ is forced at zero ($\theta_r(t) = 0$, $\forall t \in \mathbb{T}$). Figure (11) shows the evolutions of the fixed points of the autonomous dynamic system $\mathcal{S}^{pheno}$ with respect to friction coefficient $\mu_{s_2-r_2}$. No difference compared to **cases 1** and **2** is observed. Then, the stability analyses of the calculated fixed points are performed and the evolutions of the real and imaginary parts (eigenfrequencies $f = \frac{Im(\lambda)}{2\pi}$) of the eigenvalues with respect to friction coefficient $\mu_{s_2-r_2}$ at interface $(s_2 - r_2)$ are plotted in figure (12). The first difference with **cases 1** and **2** concerns the bifurcation points for $\beta = 1°$ and $\beta = 1.75°$, which have decreased overall. Moreover, the translation mode of stator s_2 does not appear, which makes sense given that link $(s_1 - s_2)$ is blocked. Finally, the temporal integrations initiated from three points associated with three inclination angles β (0, 1 and 1.75 °) are represented in figure (13) for a coefficient of friction $\mu_{s_2-r_2}$. When the rotation angle is null, the Whirl mode appears for each inclination angle β.
In a second phase, the system is forced ($\theta_r(t) = \omega\, t$, $\forall t \in \mathbb{T}$). The same temporal integrations as previously are carried out and the temporal evolutions of generalized coordinates are presented in figure (14). The major difference with the case where rotation angle $\theta_r(t)$ is forced at zero is that a Whirl mode no longer appears for an angle β of 1.75°. In addition, the levels of the limit cycles are lower and it is possible to distinguish a frequency associated with rotation angle $\theta_r(t)$ in the temporal evolution of the generalized coordinate $q_6(t)$. For the generalized coordinates $q_1(t)$ and $q_2(t)$, the same frequency is observed but is multiplied by two. When the angle of rotation $\theta_r(t)$ of the rotor r_1 is $\pi + \epsilon\,\pi$, $\epsilon \in \mathbb{Z}$, the rotor disc r_2, which moves in the direction z" of the cartesian coordinate system $\mathcal{R}_2 = \left(O_3(t), \boldsymbol{e_1^{r_1}}(t), \boldsymbol{e_2^{r_1}}(t), \boldsymbol{e_3^{r_1}}(t)\right)$ describes an elliptical trajectory in the global cartesian coordinate system $\mathcal{R}_0 = (O, \boldsymbol{e_1}, \boldsymbol{e_2}, \boldsymbol{e_3})$. This closed cycle is performed twice when the rotor r_1 has turned one revolution ($\theta_r(t) = 2\,\pi$). At each half-turn and through the contact with friction at the interface $s_2 - r_2$, the movement of the rotor r_2 is transmitted to the stator s_2 which transmits it to s_1 then to the beam b. A cycle of period $\frac{\pi}{\omega_r}$ can be observed through the generalized coordinates $q_1(t)$ and $q_2(t)$. This means that taking into account the difference j_2 in the link $(r_1 - r_2)$ (movement of the rotor discs r_2 radially), is very important. An orbital stability study is then carried out by varying the friction coefficient $\mu_{s_2-r_2}$ in a range from 0 to 1. The Monodromy matrix is calculated for this same range and the eigenvalues are plotted in the complex plane, as shown in figure (15). The transervation of the visible unit circle T corresponds to the bifurcation of *Neimark-Saker* or secondary *Hopf*. Figure (16) (respectively (17)) shows the temporal evolutions of the generalized coordinates for a value of the friction coefficient located before (resepctively after) the critical value inducing a bifurcation: $\mu_{s_2-r_2} = 0.1$ (respectively $\mu_{s_2-r_2} = 0.3$). Before the bifurcation, a limit cycle with a frequency corresponding to the rotation of the rotor disc r_1, is visible for each generalized coordinate $q_i(t)$, $i = \{1; 2; 6\}$. The frequency associated with $q_6(t)$ corresponds to the frequency rotation of r_1 and those of $q_1(t)$ and $q_2(t)$ at half this frequency. This observation was justified previously. After the bifurcation, the amplitudes associated with Whirl instability appear around the cycle associated with the rotor rotation and are visible on each temporal evolution of the generalized coordinates $q_i(t)$, $i = \{1; 2; 6\}$. The value of $\mu_{s_2-r_2}$, for which the system presents a *Hopf* bifurcation, is clearly visible in figure (15) (about 0.2). Consequently, for an inclination angle $\beta = 1°$, a small difference appears in the limit cycle amplitude (figure (2) between the autonomous and forced systems, but the bifurcation occurs for the same coefficient of friction (about 0.2), as shown in figures (12) and (15). Finally, the same analyses are performed with an angle β of 1.75° and

presented in figures (18), (19) and (20). With an angle $\beta = 1.75°$, the critical friction coefficient μ determined by fixed point stability analysis (rotation angle θ_r forced at zero) is different from that determined by a orbital stability analysis (rotation of the rotor disc $\theta_r = \omega_r t$, $t \in \mathbb{T}$) and is about 0.65 instead of 0.45. The observations that can be made on the figures (19) and (20) are the same as for an inclination angle β of 1 °. Nevertheless, a small difference appears on the temporal evolutions of the generalized coordinates after bifurcation. Indeed , the instability is less visible on $q_6(t)$ and the amplitudes of $q_1(t)$ and $q_2(t)$ are greater.

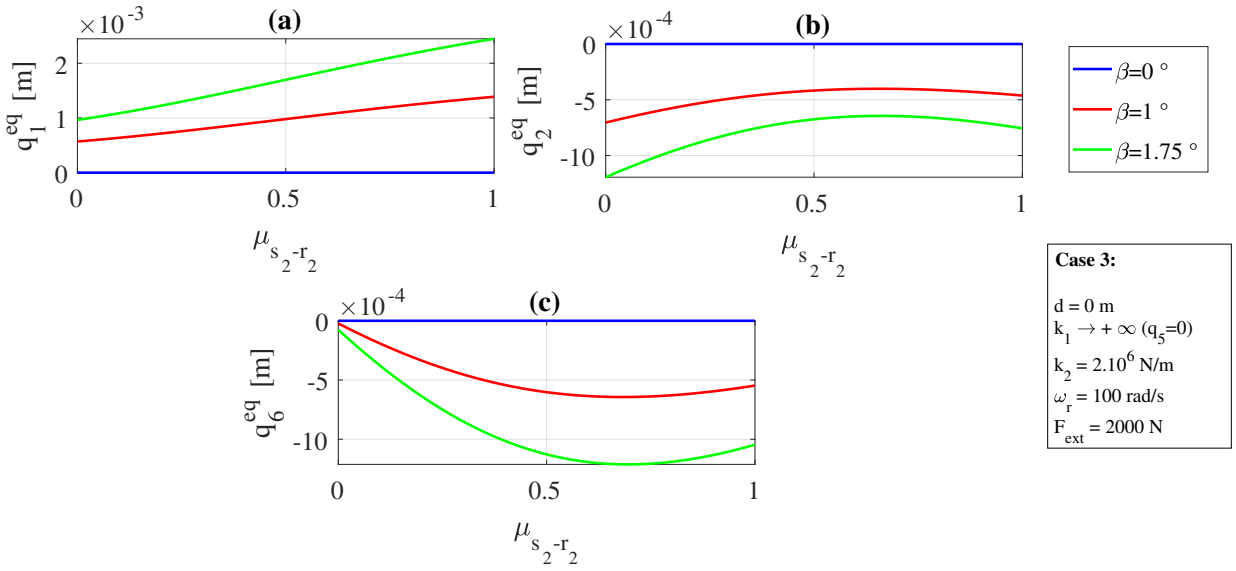

Figure 11: Evolution of fixed points $\boldsymbol{X_e}$ of dynamical system $\mathcal{S}^{pheno}$ with respect to friction coefficient $\mu_{s_2-r_2}$ for **case 3** ($k_1 \rightarrow +\infty$, $k_2 \rightarrow +\infty$, $\omega_r = 100$ rad/s, $F_{ext} = 2000N$), a center distance $d_1 = 0$ and 3 values of angle β ($\beta = 0$, 1 and 1.75 °). (a) Generalized coordinate q_1^{eq}. (b) Generalized coordinate q_2^{eq}. (c) Generalized coordinate q_6^{eq}.

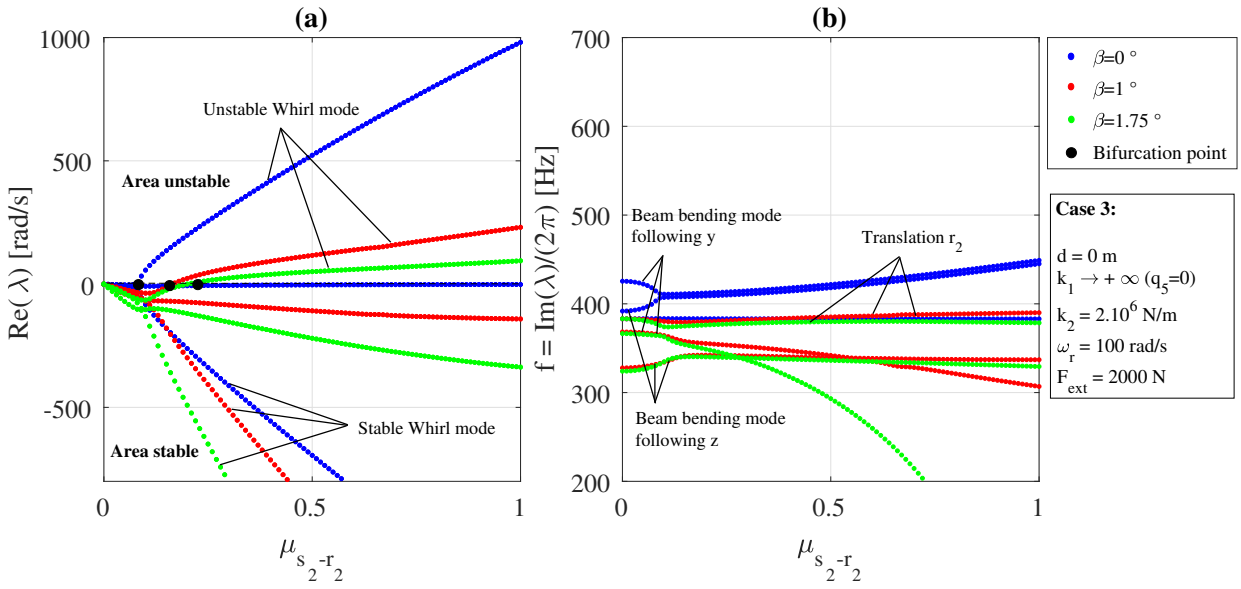

Figure 12: Evolution of eigenvalues λ with respect to friction coefficient $\mu_{s_2-r_2}$ for **case 3** ($k_1 \to +\infty$, $k_2 \to +\infty$, $\omega_r = 100$ rad/s, $F_{ext} = 2000N$), a center distance $d_1 = 0$ and 3 values of angle β ($\beta = 0$, 1 and 1.75 °). (a) Real part of eigenvalues $Re(\lambda)$. (b) Eigenfrequencies $f = \frac{Im(\lambda)}{2\pi}$.

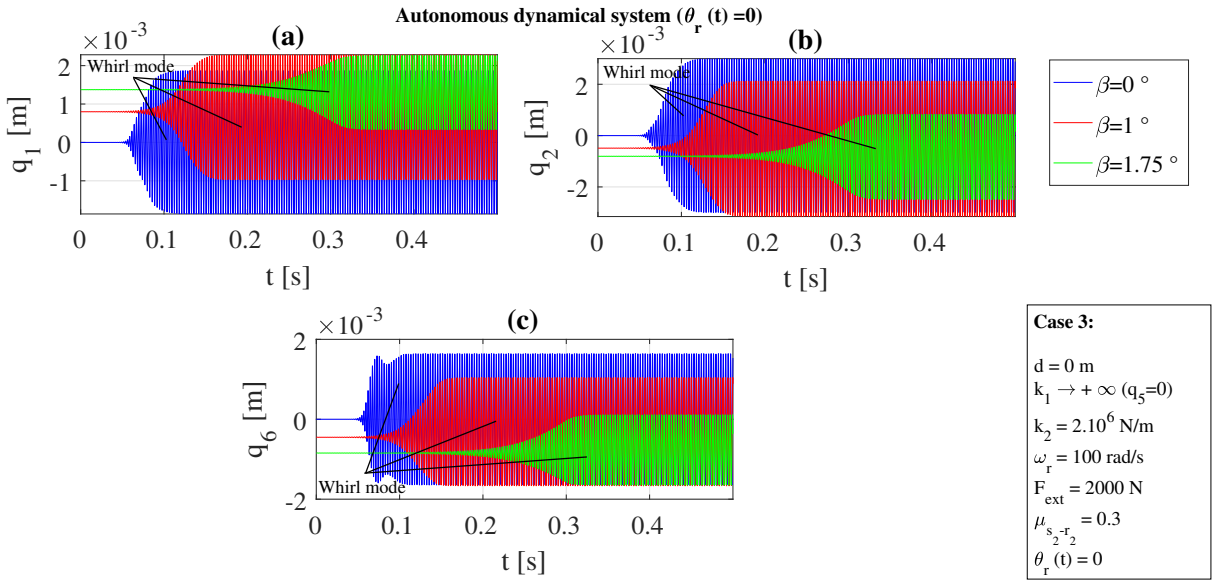

Figure 13: Temporal evolution of the dynamical system state $\boldsymbol{X}$ for **case 3** ($k_1 \to +\infty$, $k_2 \to +\infty$, $\omega_r = 100$ rad/s, $F_{ext} = 2000N$), a center distance $d_1 = 0$ and 3 values of angle β ($\beta = 0$, 1 and 1.75 °) and with rotor disc rotation ($\theta_r(t) = 0\ \forall t \in \mathbb{T}$). (a) Generalized coordinate $q_1(t)$. (b) Generalized coordinate $q_2(t)$.(c) Generalized coordinate $q_6(t)$.

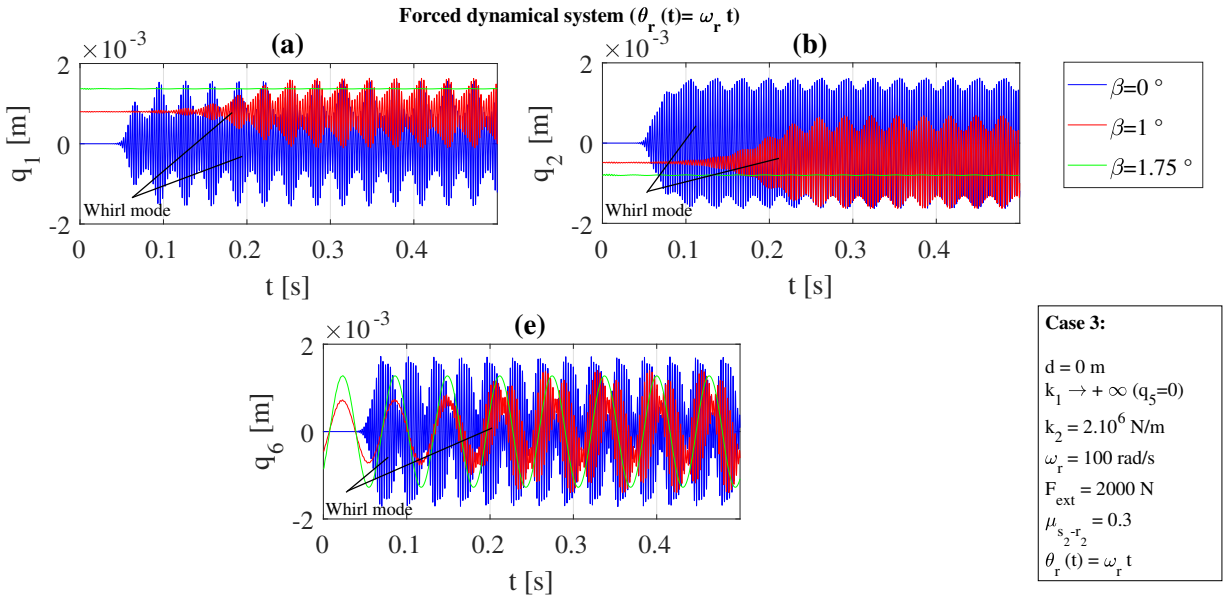

Figure 14: Temporal evolution of the dynamical system state $\boldsymbol{X}$ for **case 3** ($k_1 \rightarrow +\infty$, $k_2 \rightarrow +\infty$, ω_r = 100 rad/s, F_{ext} = 2000N), a center distance d_1 = 0, 3 values of angle β (β = 0, 1 and 1.75 °) and with rotor disc rotation ($\theta_r(t) = \omega_r\, t$). (a) Generalized coordinate $q_1(t)$. (b) Generalized coordinate $q_2(t)$. (c) Generalized coordinate $q_6(t)$.

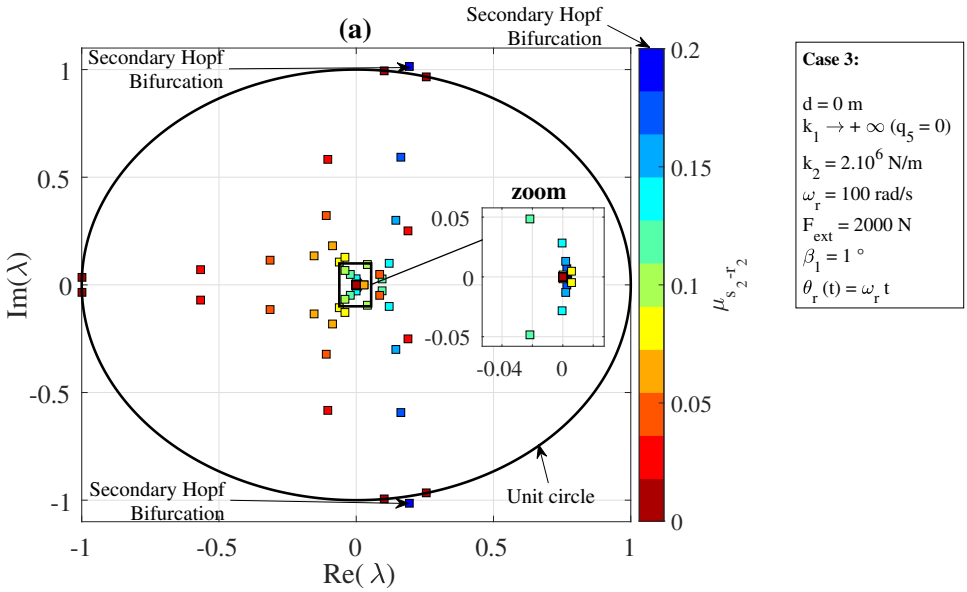

Figure 15: Evolution of Monodromy matrix eigenvalues in the complex plane with respect to friction coefficient ($\mu_{s_2-r_2} \in \{0; 0.02; ...; 1\}$) for **case 3** ($k_1 \rightarrow +\infty$, $k_2 \rightarrow +\infty$, ω_r = 100 rad/s, F_{ext} = 2000N), a center distance d_1 = 0, an angle β = 1°. (a) Eigenvalues of $\boldsymbol{M_{cycle}}$. (b) Period T_r of generalized coordinate $q_1(t)$. (c) Period T_r of generalized coordinate $q_2(t)$. (d) Period T_r of generalized coordinate $q_6(t)$.

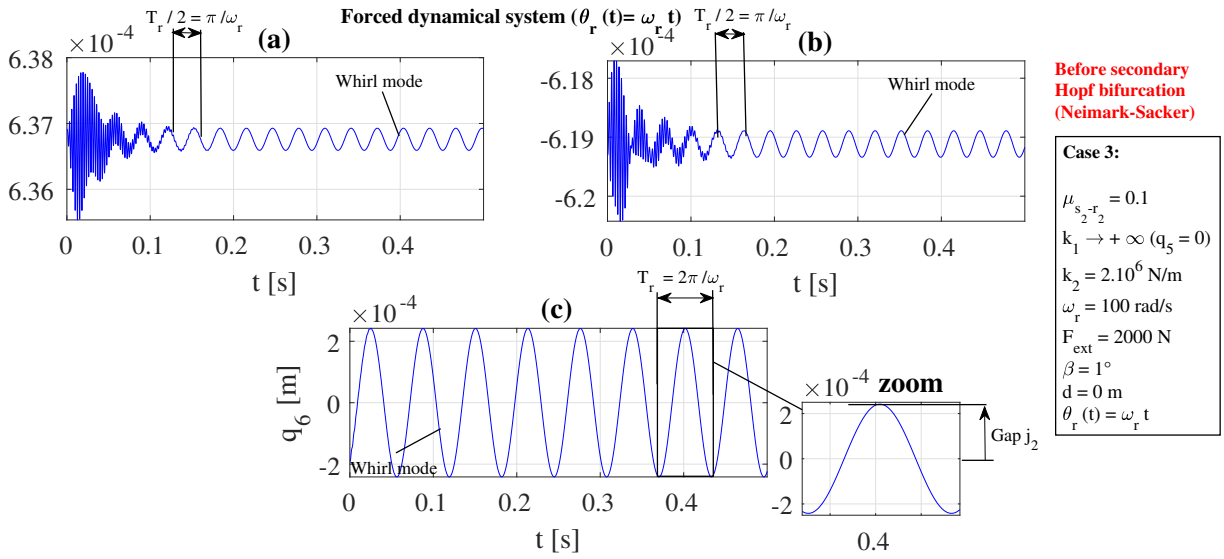

Figure 16: Temporal evolution of the dynamical system state $\boldsymbol{X}$ for **case 3** ($k_1 \rightarrow +\infty$, $k_2 \rightarrow +\infty$, ω_r = 100 rad/s, F_{ext} = 2000N), a center distance $d_1 = 0$, an angle $\beta = 1°$, a friction coefficient rank ($\mu_{s_2-r_2} \in \{0; 0.02; ...; 1\}$) and with rotor disc rotation ($\theta_r(t) = \omega_r\, t$). (a) Generalized coordinate $q_1(t)$. (b) Generalized coordinate $q_2(t)$. (c) Generalized coordinate $q_6(t)$.

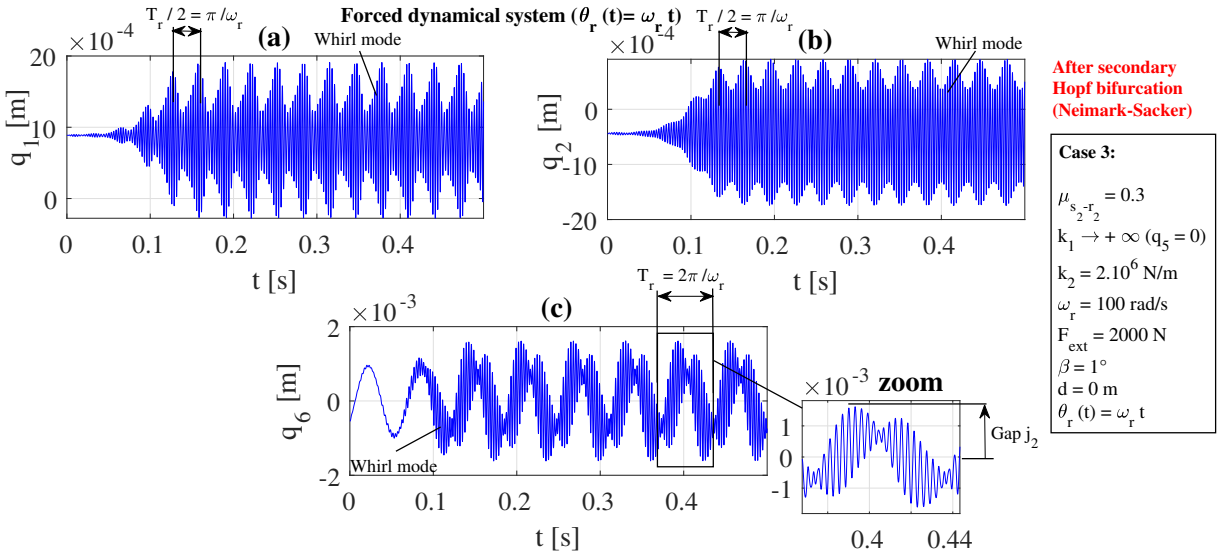

Figure 17: Temporal evolution of the dynamical system state $\boldsymbol{X}$ for **case 3** ($k_1 \rightarrow +\infty$, $k_2 \rightarrow +\infty$, ω_r = 100 rad/s, F_{ext} = 2000N), a center distance $d_1 = 0$, an angle $\beta = 1°$, a friction coefficient rank ($\mu_{s_2-r_2} \in \{0; 0.02; ...; 1\}$) and with rotor disc rotation ($\theta_r(t) = \omega_r\, t$). (a) Generalized coordinate $q_1(t)$. (b) Generalized coordinate $q_2(t)$. (c) Generalized coordinate $q_6(t)$.

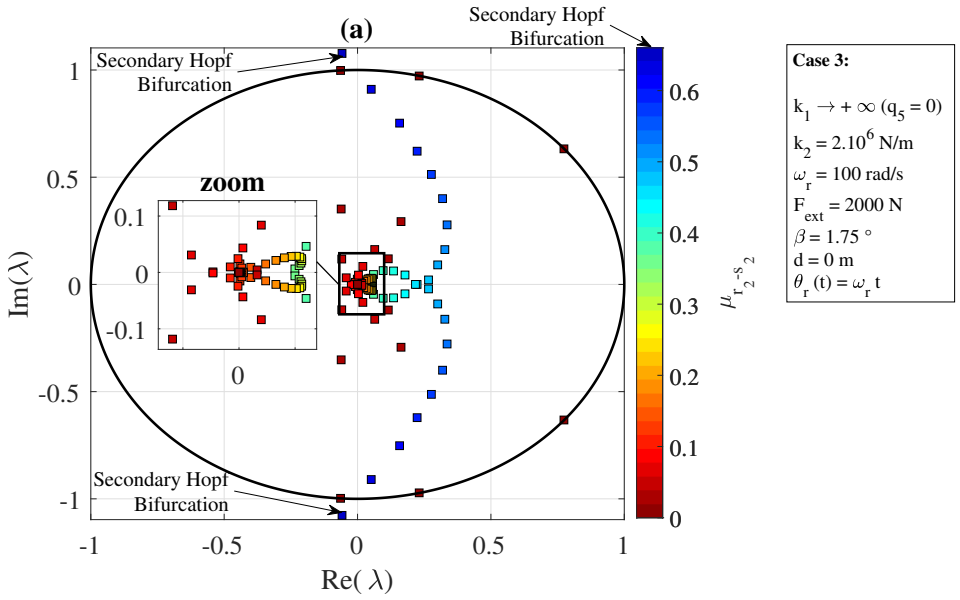

Figure 18: Evolution of Monodromy matrix eigenvalues in the complex plane with respect to friction coefficient ($\mu_{s_2-r_2} \in \{0; 0.02; ...; 1\}$) for **case 3** ($k_1 \to +\infty$, $k_2 \to +\infty$, $\omega_r = 100$ rad/s, $F_{ext} = 2000N$), a center distance $d_1 = 0$, an angle $\beta = 1.75°$. (a) Eigenvalues of $\boldsymbol{M_{cycle}}$. (b) Period T_r of generalized coordinate $q_1(t)$. (c) Period T_r of generalized coordinate $q_2(t)$. (d) Period T_r of generalized coordinate $q_6(t)$.

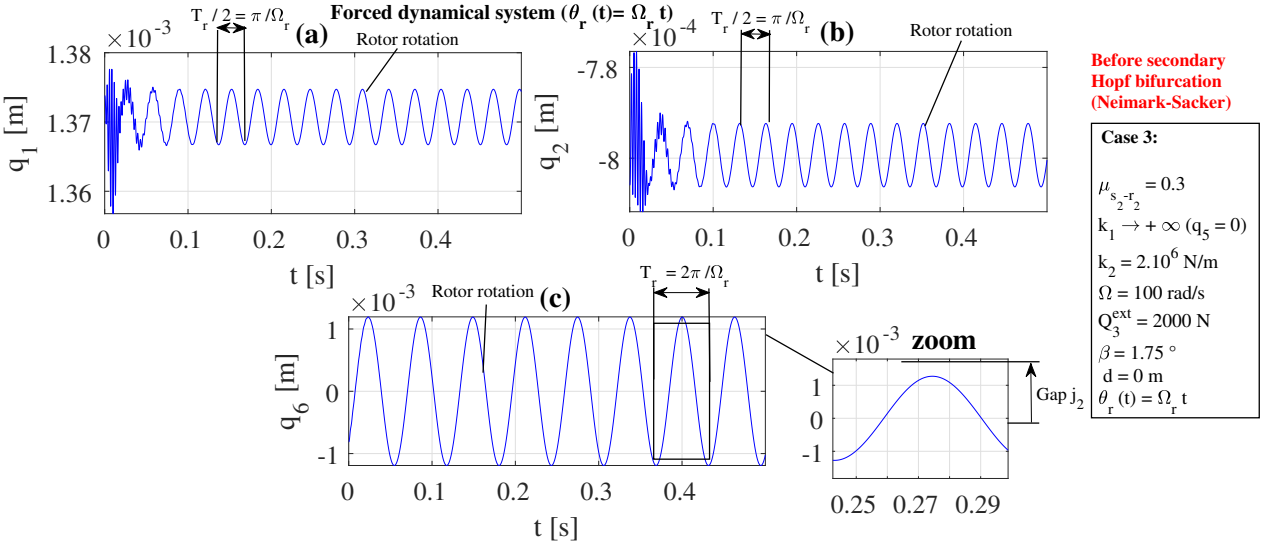

Figure 19: Temporal evolution of the dynamical system state $\boldsymbol{X}$ for **case 3** ($k_1 \to +\infty$, $k_2 \to +\infty$, $\omega_r = 100$ rad/s, $F_{ext} = 2000N$), a center distance $d_1 = 0$, an angle $\beta = 1.75°$, a friction coefficient rank ($\mu_{s_2-r_2} \in \{0; 0.02; ...; 1\}$) and with rotor disc rotation ($\theta_r(t) = \omega_r\, t$). (a) Generalized coordinate $q_1(t)$. (b) Generalized coordinate $q_2(t)$. (c) Generalized coordinate $q_6(t)$.

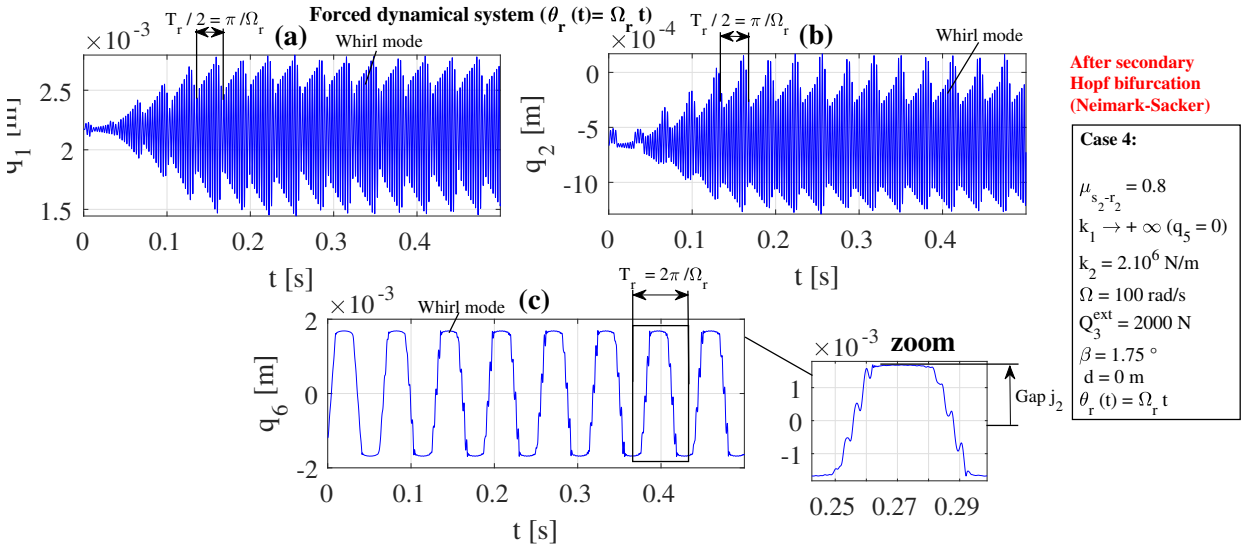

Figure 20: Temporal evolution of the dynamical system state $\boldsymbol{X}$ for **case 3** ($k_1 \rightarrow +\infty$, $k_2 \rightarrow +\infty$, $\omega_r = 100$ rad/s, $F_{ext} = 2000N$), a center distance $d_1 = 0$, an angle $\beta = 1.75°$, a friction coefficient rank ($\mu_{s_2-r_2} \in \{0; 0.02; ...; 1\}$) and with rotor disc rotation ($\theta_r(t) = \omega_r\, t$). (a) Generalized coordinate $q_1(t)$. (b) Generalized coordinate $q_2(t)$. (c) Generalized coordinate $q_6(t)$.

In **case 4**, in addition to unblocking link $(s_1 - s_2)$, link $(r_1 - r_2)$ is unblocked. For the same reasons mentioned in **case 3**, the search for a fixed point for a non-autonomous dynamical system makes no sense. This is a forced dynamic system whose forcing corresponds to rotation angle $\theta_r(t)$ of rotor disc r_1.

As for the previous case, in a first phase, rotation angle $\theta_r(t)$ is forced to zero for each time $t \in \mathbb{T}$. This allows one to make a comparison with the case where the system is forced. The calculations of fixed points and the analysis of their stability are done with the same values of parameters as in the previous case and are presented in figures (21) and (22). Concerning the evolution of the fixed points, there is no difference with the previous cases and in particular **cases 2** and **3** which respectively contain link $(s_1 - s_2)$ and $(r_1 - r_2)$ unblocked. For the stability study, the first difference with **case 3** concerns the bifurcation points for angles $\beta = 1$ and $= 1.75°$, which are greater. Moreover, a coalescence of eigenfrequencies appears for an angle $\beta = 1°$. Finally, the translation mode of rotor disc r_2 is visible in figure (22) and the associated frequencies are lower than those associated with the translation mode of stator disc s_2. The temporal integrations represented in figure (23) are performede with a friction coefficient $\mu_{s_2-r_2} = 0.5$. The observations are similar to those in the previous case, i.e., the levels of the limit cycles are lower when angle β is large.

In a second phase, rotation angle $\theta_t(t)$ of rotor disc r_1 is no longer forced to zero. Figure (24) shows the temporal evolution of each generalized coordinate in the case where the dynamical system is forced. A first important difference appears concerning the rotor rotation, which is visible for the generalized coordinate $q_6(t)$ where angle β is null. This rotor rotation is also visible on the generalized coordinates $q_1(t)$ and $q_2(t)$, but it is multiplied by two. Moreover, unlike in **case 3** where the system is forced, the whirl mode which appears for an angle $\beta = 1$ no longer appears, as the figures show (23) and (24). It would therefore seem that the bifurcation point for the parameters considered (here $\mu_{s_2-r_2}$) is no longer the same when the system is forced. To verify these observations, an orbital stability study is carried out by changing the friction coefficient $\mu_{s_2-r_2}$ and for the same values of the other parameters. Figure (25) presents the values of the Monodromy matrix for each coefficient of friction $\mu_{s_2-r_2}$ in a range from 0 to 1. The crossing of the unit circle C for conjugated complex values (for $\mu = 0.6$) indicates that it is a secondary *Hopf* bifurcation or a *Neimark-Saker*, as in **case 3**. This bifurcation is of codimension 1, given that it can appear by having only friction coefficient $\mu_{s_2-r_2}$ vary. Figure (26) (respectively (27)) presents the temporal evolutions of the generalized coordinates for a value of friction coefficient $\mu_{s_2-r_2}$ located before (respectvively after) the critical value (about 0.6) for which the dynamic system $\mathcal{S}^{pheno}$ presents a *Neimark-Sacker* bifurcation. These temporal integrations are initiated from fixed points associated with the load of rotor disc F_{ext},for an angle $\beta = 1$ and for a rotation angle $\theta_4(t)$ of rotor disc r_1 which is null. In conclusion, the system presents a bifurcation for a value of $\mu_{s_2-r_2}$ around 0.6. There is thus a difference of 0.2 compared to the $\mu_{s_2-r_2}$ of 0.4 in the case where rotation angle $\theta_4(t)$ is fixed to zero. The difference in the critical

coefficient of friction $\mu_{s_2-r_2}$ between the cases with and without rotation shows that with the existence of this closed cycle, classical studies of fixed point stability no longer make sense and must be replaced by studies of orbital stability. Indeed, these studies will be over-predictive and the mechanical systems studied will be oversized.

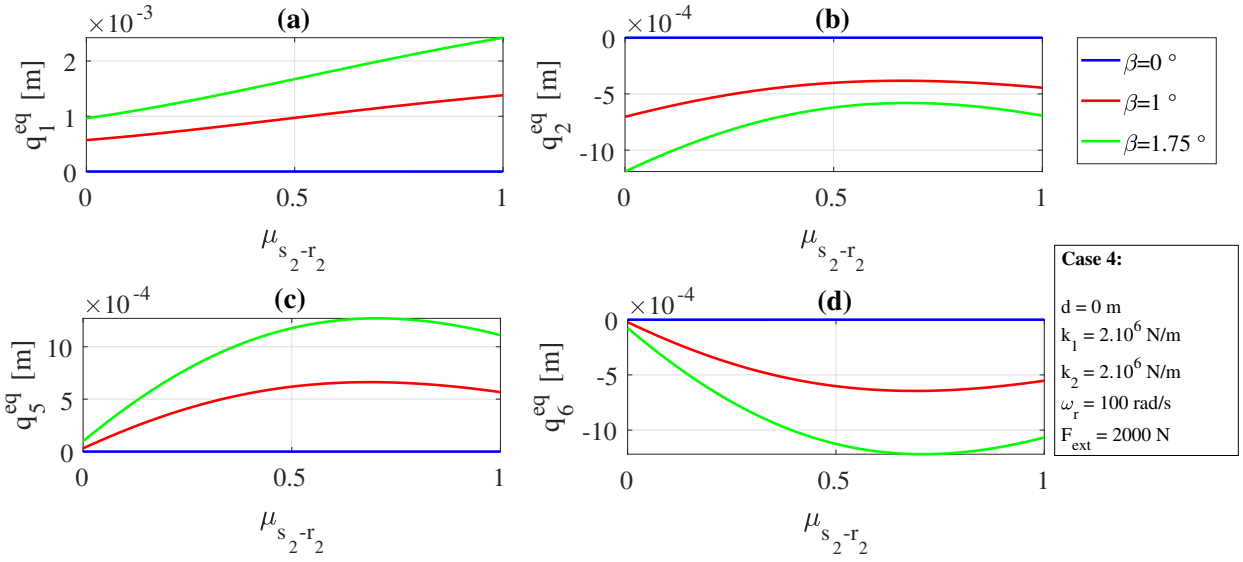

Figure 21: Evolution of fixed points $\boldsymbol{X_e}$ of dynamical system $\mathcal{S}^{pheno}$ with respect to friction coefficient $\mu_{s_2-r_2}$ for **case 4** ($k_1 \to +\infty$, $k_2 \to +\infty$, $\omega_r = 100$ rad/s, $F_{ext} = 2000N$), a center distance $d_1 = 0$ and 3 values of angle β ($\beta = 0$, 1 and 1.75 °). (a) Generalized coordinate q_1^{eq}. (b) Generalized coordinate q_2^{eq}. (c) Generalized coordinate q_5^{eq}. (d) Generalized coordinate q_6^{eq}.

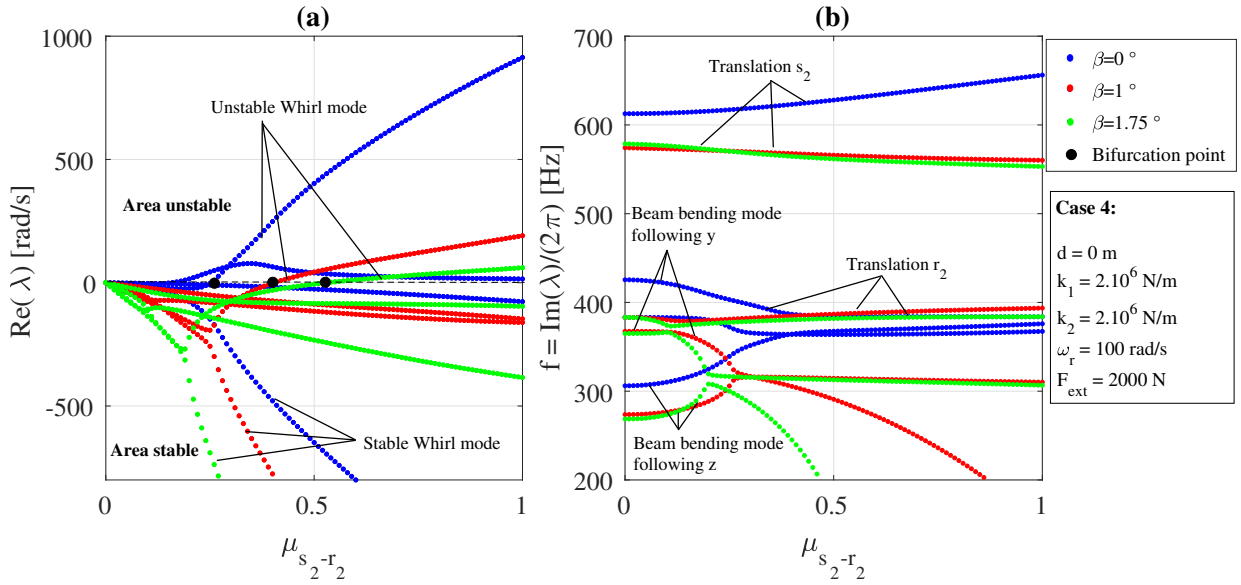

Figure 22: Evolution of eigenvalues λ with respect to friction coefficient $\mu_{s_2-r_2}$ for **case 4** ($k_1 \to +\infty$, $k_2 \to +\infty$, $\omega_r = 100$ rad/s, $F_{ext} = 2000N$), a center distance $d_1 = 0$ and 3 values of angle β ($\beta = 0$, 1 and 1.75 °). (a) Real part of eigenvalues $Re(\lambda)$. (b) Eigenfrequencies $f = \frac{Im(\lambda)}{2\pi}$.

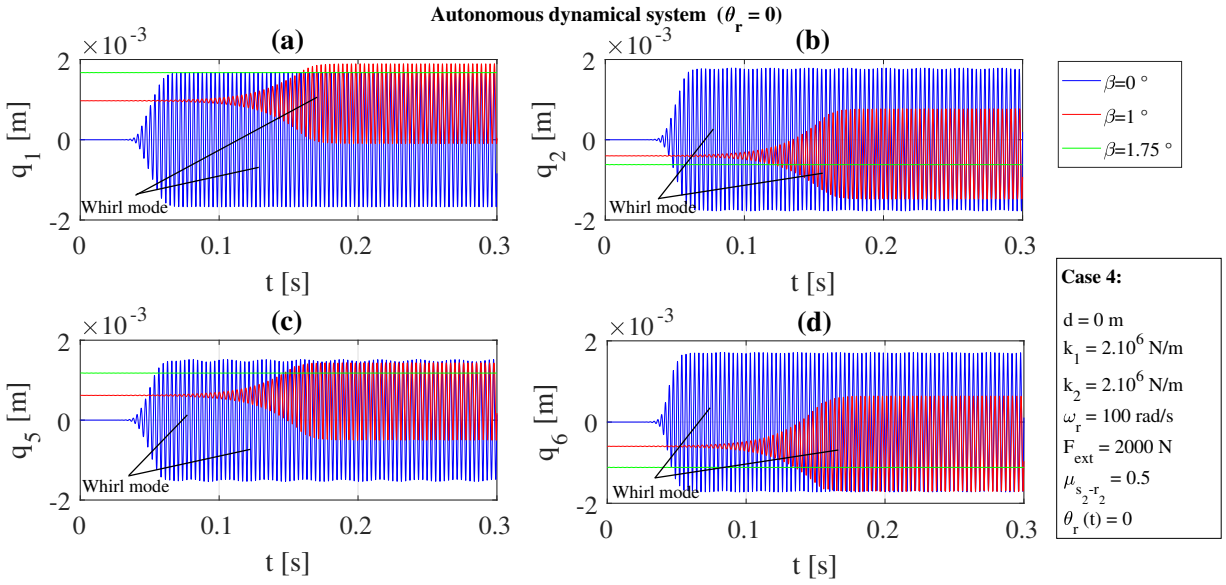

Figure 23: Temporal evolution of the dynamical system state $\boldsymbol{X}$ for **case 4** ($k_1 \to +\infty$, $k_2 \to +\infty$, ω_r = 100 rad/s, $F_{ext} = 2000N$), a center distance $d_1 = 0$, 3 values of angle β (β = 0, 1 and 1.75 °) and without rotor disc rotation ($\theta_r(t) = 0\ \forall t \in \mathbb{T}$). (a) Generalized coordinate $q_1(t)$. (b) Generalized coordinate $q_2(t)$. (c) Generalized coordinate $q_5(t)$. (d) Generalized coordinate $q_6(t)$.

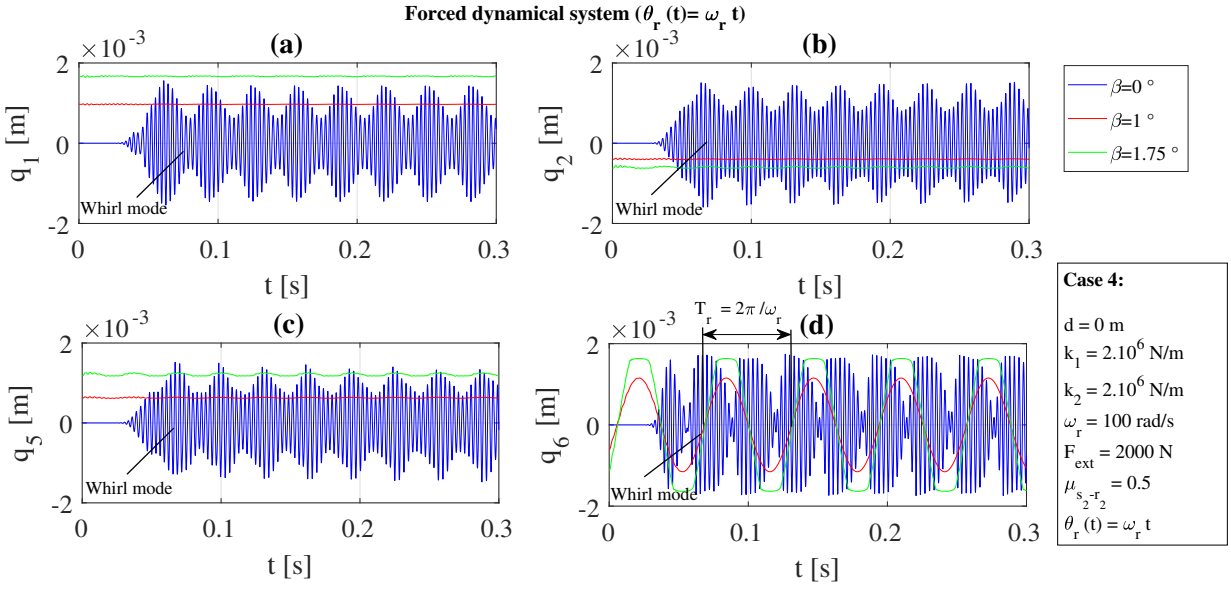

Figure 24: Temporal evolution of the dynamical system state $\boldsymbol{X}$ for **case 4** ($k_1 \to +\infty$, $k_2 \to +\infty$, ω_r = 100 rad/s, $F_{ext} = 2000N$), a center distance $d_1 = 0$, 3 values of angle β (β = 0, 1 and 1.75 °) and with rotor disc rotation ($\theta_r(t) = \omega_r\, t$). (a) Generalized coordinate $q_1(t)$. (b) Generalized coordinate $q_2(t)$. (c) Generalized coordinate $q_5(t)$. (d) Generalized coordinate $q_6(t)$.

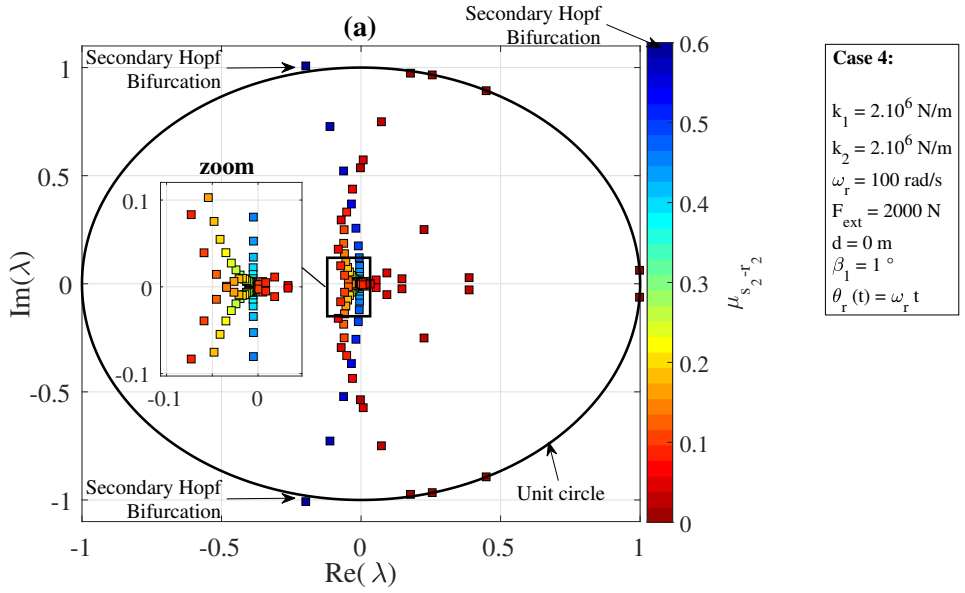

Figure 25: Evolution of Monodromy matrix eigenvalues in the complex plane with respect to friction coefficient ($\mu_{s_2-r_2} \in \{0; 0.02; ...; 1\}$) for **case 4** ($k_1 \to +\infty$, $k_2 \to +\infty$, $\omega_r = 100$ rad/s, $F_{ext} = 2000N$), a center distance $d_1 = 0$, an angle $\beta = 1°$. (a) Eigenvalues of $\boldsymbol{M_{cycle}}$. (b) Period T_r of generalized coordinate $q_1(t)$. (c) Period T_r of generalized coordinate $q_2(t)$. (d) Period T_r of generalized coordinate $q_5(t)$. (e) Period T_r of generalized coordinate $q_6(t)$.

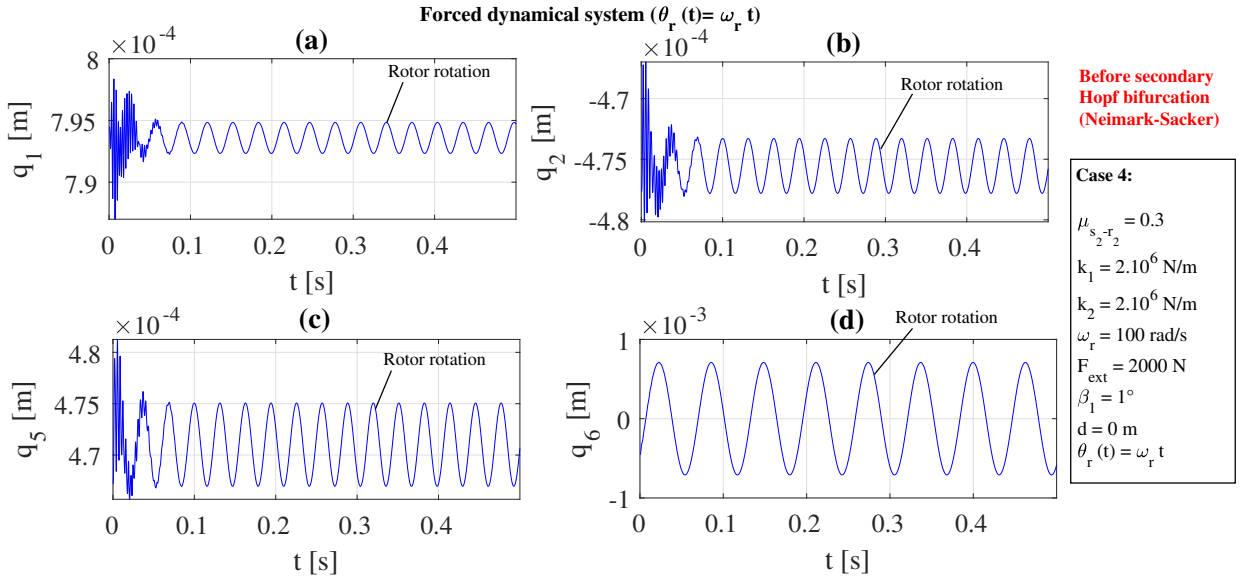

Figure 26: Temporal evolution of the dynamical system state $\boldsymbol{X}$ for **case 4** ($k_1 \to +\infty$, $k_2 \to +\infty$, $\omega_r = 100$ rad/s, $F_{ext} = 2000N$), a center distance $d_1 = 0$, an angle $\beta = 1°$, a friction coefficient rank ($\mu_{s_2-r_2} \in \{0; 0.02; ...; 1\}$) and with rotor disc rotation ($\theta_r(t) = \omega_r t$). (a) Generalized coordinate $q_1(t)$. (b) Generalized coordinate $q_2(t)$. (c) Generalized coordinate $q_5(t)$. (d) Generalized coordinate $q_6(t)$.

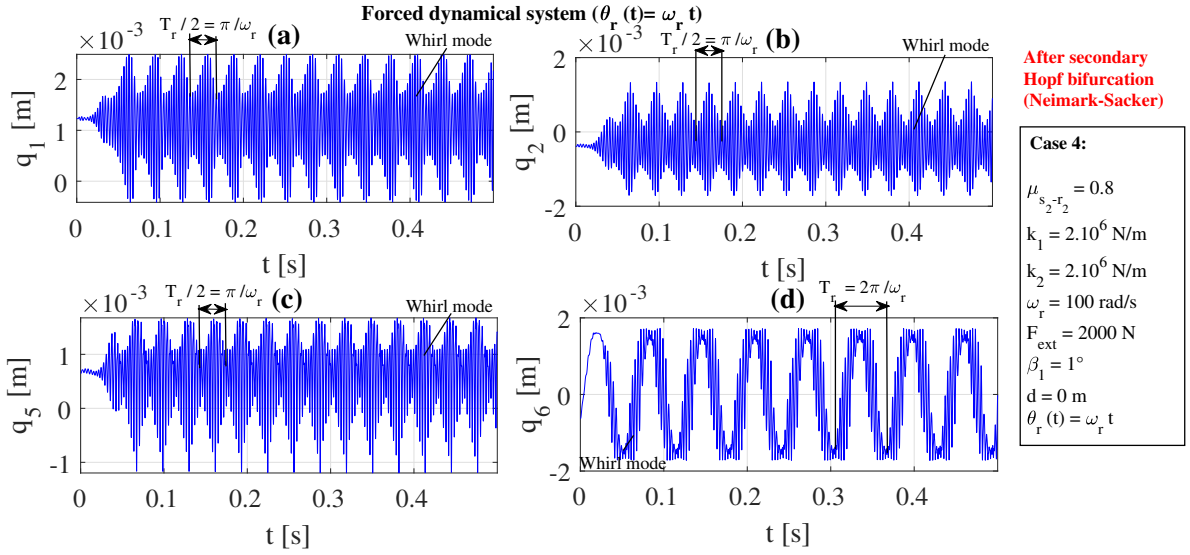

Figure 27: Temporal evolution of the dynamical system state $\boldsymbol{X}$ for **case 4** ($k_1 \to +\infty$, $k_2 \to +\infty$, $\omega_r = 100$ rad/s, $F_{ext} = 2000N$), a center distance $d_1 = 0$, an angle $\beta = 1°$, a friction coefficient rank ($\mu_{s_2-r_2} \in \{0; 0.02; ...; 1\}$) and with rotor disc rotation ($\theta_r(t) = \omega_r\, t$). (a) Generalized coordinate $q_1(t)$. (b) Generalized coordinate $q_2(t)$. (c) Generalized coordinate $q_5(t)$. (d) Generalized coordinate $q_6(t)$.

5. Conclusion

The main objective of this paper was to study the influence of three geometrical imperfections on the stability and the behavior of a phenomenological model describing the generalized design of many mechanical systems. These are mainly mechanical systems composed of two parts (stationary and rotating) and exhibiting vibratory instabilities induced by friction. The first imperfection studied is the gaps j_1 and j_2 located in the links serving to connect the rotor and stator discs to the structure of the studied system. In the model presented, only radial gaps are modeled (links $(s_1 - s_2)$ and $(r_1 - r_2)$). The second imperfection is a center distance d between the axis of the stationary part (first part s_1 of stator disc s) and that of the rotating part (first part r_1 of rotor disc r). The thrid imperfection is an inclination of the rotating part (rotor disc r) by an inclination angle called β.

Firstly, the mechanical problem and associated hypotheses were presented in their entirety. Next, the equations of motion were written by means of a Lagrangian approach including a *Rayleigh-Ritz* method for the spatial discretization of the beam. All developments and simplifications of the equations are detailed in Annexes A and B. Among these simplications, the contacts with friction at interfaces $(s_1 - s_2)$ and $(r_1 - r_2)$ were simplified by means of two nonlinear laws described in Annex B.

Secondly, a parametric study was carried out to analyze the influence of imperfections on the stability and the dynamic behavior of the system. Since there is a large difference in unstable behaviors between a gap located at link $(s_1 - s_2)$ and a gap located at link $(r_1 - r_2)$, this study was divided into two parts, each comprising two cases. In the first part, **cases 1** and **2** were studied, and for each, link $(r_1 - r_2)$ is always considered blocked. Consequently, the dynamic system is not forced and the stability analyses could be done by analyzing the fixed points. In conclusion to this first part of the study, the center distance d has very little influence on the stability of fixed points but it would have an influence if there were very high values which have little physical meaning. The temporal integrations initiated from these fixed points also showed a very slight influence of the center distance parameter on the dynamic behavior, in particular the amplitudes of the limit cycles. Nevetheless, the inclination angle β has a strong influence on the fixed points and their stability. The values of friction coeffcient $\mu_{s_2-r_2}$ for which dynamic system $\mathcal{S}^{pheno}$ presents a *Hopf* bifurcation are globally weaker when link $(s_1 - s_2)$ is blocked. Finally, the amplitudes of the limit cycles are lower with an increase in angle β. In the second part, **cases 3** and **4** were studied, and for each, link $(r_1 - r_2)$ is unblocked. Therefore, given that the system becomes non-autonomous, stability analyses were carried out on periodic orbits by constructing, for several values of the coefficient of friction $\mu_{s_2-r_2}$, the associated Monodromy matrix. The period of

these orbits corresponds to that of rotor disc r_1. However, in order to compare these orbital stability analyses, fixed point studies, which don't take into account the rotation effect were also performed. The main observation concerns large differences in the values of critical friction coefficient $\mu_{s_2-r_2}$, which were found between the fixed point and orbital stability analyses. In particular, it clearly appears that the gap in the links coupled with the inclination of the rotating part (rotor disc r) is responsible for these differences. This is an interesting result, demonstrating the importance of modeling these phenomena even if calculation times increase and stability analyses are more technical to perform.

Annexe A: Expressions of kinetic and potential energies

For any time $t \in \mathbb{T} = [0, t_{max}]$, the expressions of the kinetic and potential energies of the beam are denoted $\mathcal{T}_{b/R_0}(t)$ and $\mathcal{V}_b(t)$. They are associated with the movement of bending following directions y and z and are expressed in the reference inertial frame R_0 thanks to the cartesian coordinate system $\mathcal{R}_0$:

$$\forall t \in \mathbb{T}, \begin{cases} \mathcal{T}^b_{/R_0}(t) = \dfrac{1}{2}\rho \sum\limits_{i=2}^{3} I_i^b \int_0^L \left(\dfrac{\partial \dot{u}^b_{i/R_0}(\boldsymbol{x},t)}{\partial x} \right)^2 dx + \dfrac{1}{2}\rho S^b \sum\limits_{i=2}^{3} \int_0^L \left(\dot{u}^b_{i/R_0}(\boldsymbol{x},t) \right)^2 dx \\ \qquad\qquad = \dfrac{1}{2}\left(\dfrac{4}{3}\dfrac{\rho I_3^b}{L} + \dfrac{L}{5}\rho S^b \right) \dot{q_1}^2(t) + \dfrac{1}{2}\left(\dfrac{4}{3}\dfrac{\rho I_2^b}{L} + \dfrac{L}{5}\rho S^b \right) \dot{q_2}^2(t) \\ \mathcal{V}^b_{/R_0}(t) = \dfrac{1}{2} E^b \sum\limits_{i=2}^{3} I_i^b \int_0^L \left(\dfrac{\partial^2 u_i^b(\boldsymbol{x},t)}{\partial x^2} \right)^2 dx = \dfrac{1}{2}\dfrac{4}{L^3} I_3^b E\, q_1^2(t) + \dfrac{1}{2}\dfrac{4}{L^3} I_2^b E\, q_2^2(t) + \dfrac{2}{3}\dfrac{GC}{L} q_4^2(t) \end{cases} \tag{A.1}$$

with:

- $S^b = b\,h$, the beam section.
- $I_2^b = \int_{S_b} z^2\, dS_b = \frac{b h^3}{12}$ (respectively $I_3^b = \int_{S_b} y^2\, dS_b = \frac{b^3 h}{12}$), the area moment of inertia ofhe beam b around direction y (respectively direction z).

The kinetic energies of stator discs s_1 et s_2 are due to the bendings of the beam in directions y and z. The potential energy of each disc is always zero given that they are supposed to be undeformable. Rotor discs r_1 andt r_2 only have the possibility of moving in axial direction x. For any time $t \in \mathbb{T}$, the expressions of the kinetic and potential energies associated with the stator and rotor discs are denoted $\mathcal{T}_{s_1/R_0}(t)$, $\mathcal{T}_{s_2/R_0}(t)$, $\mathcal{T}_{r_1/R_0}(t)$ and $\mathcal{T}_{r_2/R_0}(t)$. They are also expressed in the reference inertial frame R_0 thanks to the cartesian coordinate system $\mathcal{R}_0$:

$$\forall t \in \mathbb{T}, \begin{cases} \mathcal{T}^{s_1}_{/R_0}(t) = \dfrac{1}{2}\rho\, e \sum\limits_{i=2}^{3} I_i^{s_1} \left(\dfrac{\partial \dot{u}_i^b(\boldsymbol{x_{O_1}},t)_{/\mathcal{R}_0}}{\partial x} \right)^2 + \dfrac{1}{2}\rho\, e\, S^s \sum\limits_{i=2}^{3} \left(\dot{u}_i^b(\boldsymbol{x_{O_1}},t)_{/\mathcal{R}_0} \right)^2 \\ \qquad\qquad = \dfrac{1}{2}\left(\rho S^s e + \dfrac{4\rho\, e\, I_z^2}{L^2} \right) \dot{q_1}^2(t) + \dfrac{1}{2}\left(\rho S_s e + \dfrac{4\rho\, e\, I_y^2}{L^2} \right) \dot{q_2}^2(t) \\ \mathcal{T}^{s_2}_{/R_0}(t) = \dfrac{1}{2}\rho\, e \sum\limits_{i=2}^{3} I_i^{s_2} \left(\dfrac{\partial \dot{u}_i^{s_2}(\boldsymbol{x_{O_2}},t)_{/\mathcal{R}_0}}{\partial x} \right)^2 + \dfrac{1}{2}\rho\, e\, S^s \sum\limits_{i=2}^{3} \left(\dot{u}_i^{s_2}(\boldsymbol{x_{O_2}},t)_{/\mathcal{R}_0} \right)^2 \\ \mathcal{T}^{r_1}_{/R_0}(t) = \dfrac{1}{2}\rho\, e\, S^r \left(\dot{u}_1^{r_1}(\boldsymbol{x_{O_3}},t)_{/\mathcal{R}_0} \right)^2 = \dfrac{1}{2}\rho\, e\, S_r\, \dot{q}_3(t)^2 \\ \mathcal{T}^{r_2}_{/R_0}(t) = \dfrac{1}{2}\rho\, e\, S^r \left(\dot{u}_1^{r_2}(\boldsymbol{x_{O_4}},t)_{/\mathcal{R}_0} \right)^2 \end{cases} \tag{A.2}$$

with:

- $S^s = \pi R_s^2$, the section of the stator discs s_1 and s_2.
- $I_2^s = \int_{S_s} z^2\, dS_s = \frac{\pi R_s^4}{4}$ (respectively $I_3^s = \int_{S_s} y^2\, dS_s = \frac{\pi R_s^4}{4}$), the area moment of inertia of stator disc s_1 and s_2, around direction y (respectively direction z).

Annexe B: Expressions of generalized forces

Interface $(s_2 - r_2)$ composed of A_{s_2} and A_{r_2}, presents a contact with friction. In this model and taking into account the freedoms of each disc, it seems judicious that boundary A_{s_2} of rotor disc s_2 is better suited to being master. Indeed, rotor disc s_2 is less free to move (only in axial direction x). For each point $M \in A_{s_2}$ positioned in $\boldsymbol{x}(t) \in \Gamma_{s_2}^{cf}(t)$, the nearest geometric point $\bar{M} \in A_{r_2}$ positioned in $\bar{\boldsymbol{x}}(t) \in \Gamma_{r_2}^{cf}(t)$ must be sought. Mathematically, this consists of solving the following optimization problem:

$$\bar{\boldsymbol{x}} = \underset{\boldsymbol{y}\in\Gamma_{r_2}^{cf}}{\arg\min}\{\frac{1}{2}\|\boldsymbol{x}-\boldsymbol{y}\|^2\} \iff \Delta u_n(\boldsymbol{x},t) = \underset{\boldsymbol{y}\in\Gamma_{r_2}^{cf}}{\min}\{\frac{1}{2}\|\boldsymbol{x}-\boldsymbol{y}\|^2\} \quad \forall \boldsymbol{x} \in \Gamma_{s_2}^{cf}(t) \tag{B.1}$$

For each point $M \in A_{s_2}$ of stator disc s_2 positioned in $\boldsymbol{x} \in \Gamma_{s_2}^{cf}(t)$ in the actual configuration, *Signorini* and *Coulomb* conditions are expressed in the basic $\mathcal{B}_4 = \left(\boldsymbol{e_1}^{r_2}(t), \boldsymbol{e_2}^{r_2}(t), \boldsymbol{e_3}^{r_2}(t)\right)$ as follows:

$$\forall \boldsymbol{x} \in \Gamma_{s_2}^{cf}(t) \;\; \forall t \in \mathbb{T}, \begin{cases} -\sigma_n(\boldsymbol{x},t) \in \partial\psi_{\mathbb{R}^+}(\Delta u_n(\boldsymbol{x},t)) \\ -\boldsymbol{\sigma_t}(\boldsymbol{x},t) \in \partial\psi^*_{D(\mu_{s_2-r_2}\,\sigma_n(\boldsymbol{x},t))}(\Delta\dot{\boldsymbol{u}}_{\boldsymbol{t}}(\boldsymbol{x},t)) \end{cases} \tag{B.2}$$

with:

- $\Delta u_n(\boldsymbol{x},t) = (\boldsymbol{u}^{r_2}(\boldsymbol{x_{O_4}},t) - \boldsymbol{u}^{s_2}(\boldsymbol{x_{O_2}},t) + \boldsymbol{\theta}^{r_2}(\boldsymbol{x_{O_4}},t) \wedge (\bar{\boldsymbol{x}} - \boldsymbol{x_{O_4}}) - \boldsymbol{\theta}^{s_2}(\boldsymbol{x_{O_2}},t) \wedge (\boldsymbol{x} - \boldsymbol{x_{O_2}}))\cdot -\boldsymbol{e_1}^{r_2}(t)$ (respectively $\Delta\dot{\boldsymbol{u}}_{\boldsymbol{t}}(\boldsymbol{x},t) = \left(\dot{\boldsymbol{u}}^{r_2}(\boldsymbol{x_{O_4}},t) - \dot{\boldsymbol{u}}^{s_2}(\boldsymbol{x_{O_2}},t) + \dot{\boldsymbol{\theta}}^{r_2}(\boldsymbol{x_{O_4}},t) \wedge (\bar{\boldsymbol{x}} - \boldsymbol{x_{O_4}}) - \dot{\boldsymbol{\theta}}^{s_2}(\boldsymbol{x_{O_2}},t) \wedge (\boldsymbol{x} - \boldsymbol{x_{O_2}})\right) \cdot -\boldsymbol{e_t}^{cf}(\boldsymbol{x},t)$), the normal relative displacement following the vector $-\boldsymbol{e_1}^{r_2}(t)$ (respectively the tangential relative velocity following vector $-\boldsymbol{e_t}^{cf}(\boldsymbol{x},t)$).
- $\boldsymbol{e_t}^{cf}(\boldsymbol{x},t) = \dfrac{\Delta\dot{\boldsymbol{u}}_{\boldsymbol{t}}(\boldsymbol{x},t)}{\|\Delta\dot{\boldsymbol{u}}_{\boldsymbol{t}}(\boldsymbol{x},t)\|}$, the friction direction in each point M positionned in $\boldsymbol{x}(t) \in \Gamma_{s_2}^{cf}(t)$ is expressed in the basic $\mathcal{B}_4$.
- $\sigma_n(\boldsymbol{x},t)$ (respectively $\boldsymbol{\sigma_t}(\boldsymbol{x},t)$), the normal stress or pressure following vector $-\boldsymbol{e_1}^{r_2}(t)$ (respectively the tangential stress of interface A_{s_2} on interface A_{r_2} following vector $-\boldsymbol{e_t}^{\boldsymbol{x},cf}(t)$).
- $\partial\psi_{\mathbb{R}^+}$ (respectively $\partial\psi_{D(\mu_{s_2-r_2}\,\sigma_n(\boldsymbol{x},t))}$), the sub-differential of $\psi_{\mathbb{R}^+} : \mathbb{R} \longrightarrow \mathbb{R}$ (respectively of $\psi_{D(\mu_{s_2-r_2}\,\sigma_n(\boldsymbol{x},t))} : \mathbb{R}^2 \longrightarrow \mathbb{R}$), the indicator function of $\mathbb{R}^+$ (respectively of $D(\mu_{s_2-r_2}\,\sigma_n(\boldsymbol{x},t))$). For a convex set K, ψ_K is defined as follows:
$$\psi_K(x) = \begin{cases} 0 & \text{si } \; x \in K \\ +\infty & \text{si } \; x \notin K \end{cases} \tag{B.3}$$
- $D(\mu_{s_2-r_2}\,\sigma_n(\boldsymbol{x},t)) = \left\{\boldsymbol{\sigma_t}(\boldsymbol{x},t) \in \mathbb{R}^2,\; \boldsymbol{\sigma_t}(\boldsymbol{x},t) \le \mu_{s_2-r_2}\,\sigma_n(\boldsymbol{x},t)\right\}$, the feasible set of tangential stress $\boldsymbol{\sigma_t}(\boldsymbol{x},t)$.

It is also necessary to specify that as for the reference [40, 41], the contact and the friction are simplified at interface $(s_2 - r_2)$. The main goal is to simplify the calculations which are detailed below. First of all, the contact is simplified by regularizing the multivalued potential, which gives rise to the normal stress expressed as follows:

$$\forall t \in \mathbb{T} \;\; \forall \boldsymbol{x} \in \Gamma_{s_2}^{cf}(t), \;\; \sigma_n(\boldsymbol{x},t) = \begin{cases} 0 & \text{si } \; \Delta u_n(\boldsymbol{x},t) > 0 \\ \rho_c\,\Delta u_n(\boldsymbol{x},t), \;\; \rho_c > 0 & \text{else} \end{cases} \tag{B.5}$$

Moreover, the tangential stresses and in particular the *Coulomb* law are simplified. The simplification allows one to consider that there is always sliding at interface $(s_2 - r_2)$, which amounts to neglecting the phenomenon of adhesion. Consequently, at any point the tangential stress is always located on the border of the cone of friction. These considerations can be used to write:

$$\forall t \in \mathbb{T}, \;\; \boldsymbol{\sigma_t}^{r_2}(\boldsymbol{x},t) = \mu_{s_2-r_2}\,\sigma(\boldsymbol{x},t)\,\boldsymbol{e_t}^{cf}(\boldsymbol{x},t) \;\; \forall \boldsymbol{x} \in \Gamma_{s_2}^{cf}(t) \tag{B.6}$$

Given that the normal stresses $\sigma_n(\boldsymbol{x},t)$ are zero on the detached interface part whose associated surface is denoted $\bar{\Gamma}_3^{cf,5}$, it is sufficient to directly perform the integrations associated with the generalized forces on the part in contact. Consequently, the expressions of the generalized forces at interface $(s_2 - r_2)$ are written:

$$\forall t \in \mathbb{T} \quad \forall j \in \{1;2;3;4;5\}, \begin{cases} Q_j^{s_1}(t) = -\boldsymbol{F}_{s_1/s_2} \dfrac{\partial \boldsymbol{u}^{s_1}(\boldsymbol{x}_{\boldsymbol{O_1}}, t)}{\partial q_j} \\ Q_j^{s_2}(t) = \boldsymbol{F}_{s_1/s_2} \dfrac{\partial \boldsymbol{u}^{s_2}(\boldsymbol{x}_{\boldsymbol{O_2}}, t)}{\partial q_j} \delta q_j(t) + \displaystyle\int_{\bar{\Gamma}_{s_2}^{cf}} \bar{\boldsymbol{\phi}}_{\boldsymbol{r_2}/\boldsymbol{s_2}}(\boldsymbol{x}, t) \dfrac{\partial \boldsymbol{u}^{s_2}(\boldsymbol{x}, t)}{\partial q_j} dS \\ Q_j^{r_1}(t) = -\left(\boldsymbol{F}_{r_1/r_2} + \boldsymbol{F}_{\boldsymbol{ext}}\right) \dfrac{\partial \boldsymbol{u}^{\boldsymbol{r_1}}(\boldsymbol{x}_{\boldsymbol{O_3}}, t)}{\partial q_j} \\ Q_j^{r_2}(t) = \boldsymbol{F}_{r_1/r_2} \dfrac{\partial \boldsymbol{u}^{\boldsymbol{r_2}}(\boldsymbol{x}_{\boldsymbol{O_4}}, t)}{\partial q_j} \delta q_j(t) - \displaystyle\int_{\bar{\Gamma}_{s_2}^{cf}} \bar{\boldsymbol{\phi}}_{\boldsymbol{r_2}/\boldsymbol{s_2}}(\boldsymbol{x}, t) \dfrac{\partial \boldsymbol{u}^{\boldsymbol{r_2}}(\boldsymbol{x}, t)}{\partial q_j} dS \end{cases} \tag{B.7}$$

with:

- $\boldsymbol{F_{ext}} = -F_{ext}\, \boldsymbol{e_1} \in \mathbb{R}^3$, the external forces vector.
- $\bar{\boldsymbol{\phi}}_{\boldsymbol{s_2}/\boldsymbol{r_2}}(\boldsymbol{x}, t) = -\bar{\boldsymbol{\phi}}_{\boldsymbol{r_2}/\boldsymbol{s_2}}(\boldsymbol{x}, t) = \rho_c\, \Delta u_n(\boldsymbol{x}, t)\, \boldsymbol{e}_{\boldsymbol{1}}^{\boldsymbol{r_1}} + \mu_{s_2 - r_2}\, \sigma(\boldsymbol{x}, t)\, \boldsymbol{e}_{\boldsymbol{t}}^{\boldsymbol{cf}}(\boldsymbol{x}, t) \in \mathbb{R}^3$, the stress vector at the interface $(s_2 - r_2)$.
- $\boldsymbol{F}_{s_1/s_2} = \begin{cases} k_1\, q_5(t) \text{ if } |q_5(t)| < j_1 \\ \left(1.5.10^{21} \left(|q_5(t)| - 1.5.10^{-3}\right)^4 + 2.10^6\right) q_5(t) \text{ else} \end{cases} = -\boldsymbol{F}_{s_2/s_1}$, the simplied force corresponding to the sum of two contributions: the friction forces (if $|q_5| < j_1$) and the contact forces (if $|q_5| \geq j_1$).
- $\boldsymbol{F}_{r_1/r_2} = \begin{cases} k_1\, q_6(t) \text{ if } |q_6(t)| < j_2 \\ \left(1.5.10^{21} \left(|q_6(t)| - 1.5.10^{-3}\right)^4 + 2.10^6\right) q_6(t) \text{ else} \end{cases} = -\boldsymbol{F}_{r_2/r_1}$, the simplied force corresponding to the sum of two contributions: the friction forces (if $|q_6| < j_2$) and the contact forces (if $|q_6| \geq j_2$).
- $\bar{\Gamma}_{s_2}^{cf}(t) = \left\{\boldsymbol{x} \in \Gamma_{s_2}^{cf} \mid u_n(\boldsymbol{x}, t) > 0\right\}, \forall t \in \mathbb{T}$, the area of the interface attached. The search for this contact area is fully detailed in [40, 41].

References

[1] E. Denimal, L. Nechak, J. J. Sinou, and S. Nacivet. A novel hybrid surrogate model and its application on a mechanical system subjected to friction-induced vibration. *Journal of Sound and Vibration*, 434:456–474, 2018. Publisher: Elsevier.

[2] N. M. Kinkaid, Olivier M. O'Reilly, and Panayiotis Papadopoulos. Automotive disc brake squeal. *Journal of sound and vibration*, 267(1):105–166, 2003. Publisher: Elsevier.

[3] Huajiang Ouyang, Wayne Nack, Yongbin Yuan, and Frank Chen. Numerical analysis of automotive disc brake squeal: a review. *International Journal of Vehicle Noise and Vibration*, 1(3-4):207–231, 2005. Publisher: Inderscience Publishers.

[4] A. Renault, F. Massa, B. Lallemand, and T. Tison. Experimental investigations for uncertainty quantification in brake squeal analysis. *Journal of Sound and Vibration*, 367:37–55, 2016. Publisher: Elsevier.

[5] Fabrice Chevillot, Jean-Jacques Sinou, Nicolas Hardouin, and Louis Jézéquel. Effects of damping on the speed of increase and amplitude of limit cycle for an aircraft braking system subjected to mode-coupling instability. *Archive of Applied Mechanics*, 80(9):1045–1054, 2010. Publisher: Springer.

[6] Fabrice Chevillot, Jean-Jacques Sinou, Nicolas Hardouin, and Louis Jezequel. Simulations and experiments of a nonlinear aircraft braking system with physical dispersion. *Journal of vibration and acoustics*, 132(4), 2010. Publisher: American Society of Mechanical Engineers Digital Collection.

[7] Antoine Gatt, Sébastien Besset, Louis Jézéquel, Abdelbasset Hamdi, and Jean-Frédéric Diebold. Reduction methods applied to aircraft brake squeal prediction and simulation. *Journal of Aircraft*, 54(4):1340–1349, 2017. Publisher: American Institute of Aeronautics and Astronautics.

[8] Steven Liu, James T. Gordon, and M. M. Ozbek. Nonlinear Model for Aircraft Brake Squeal Analysis: Model Description and Solution Methodology. 1996.

[9] Steven Y. Liu, James T. Gordon, and M. Akif Ozbek. Nonlinear Model for Aircraft Brake Squeal Analysis: Model Description and Solution Methodology. *Journal of Aircraft*, 35(4):623–630, July 1998.

[10] Xavier Lorang, Florence Foy-Margiocchi, Quoc Son Nguyen, and Pierre-Etienne Gautier. TGV disc brake squeal. *Journal of Sound and Vibration*, 293(3-5):735–746, 2006. Publisher: Elsevier.

[11] B. Hervé, J. Sinou, H. Mahé, and L. Jézéquel. Analysis of friction-induced self-generated vibrations originated from mode-coupling in clutches. *International Journal of Pure and Applied Mathematics*, 42(3):369, 2008. Publisher: Citeseer.

[12] Benjamin Hervé, J.-J. Sinou, Hervé Mahé, and Louis Jezequel. Analysis of squeal noise and mode coupling instabilities including damping and gyroscopic effects. *European Journal of Mechanics-A/Solids*, 27(2):141–160, 2008. Publisher: Elsevier.

[13] P. Chambrette and L. Jezequel. Stability of a beam rubbed against a rotating disc. *European journal of mechanics. A. Solids*, 11(1):107–138, 1992.
[14] Louis Jezequel and Claude-Henri Lamarque. Analysis of non-linear dynamical systems by the normal form theory. *Journal of sound and vibration*, 149(3):429–459, 1991. Publisher: Elsevier.
[15] Jérôme Didier, Jean-Jacques Sinou, and Béatrice Faverjon. Study of the non-linear dynamic response of a rotor system with faults and uncertainties. *Journal of Sound and Vibration*, 331(3):671–703, 2012. Publisher: Elsevier.
[16] Jean-Jacques Sinou and Louis Jézéquel. Mode coupling instability in friction-induced vibrations and its dependency on system parameters including damping. *European Journal of Mechanics-A/Solids*, 26(1):106–122, 2007. Publisher: Elsevier.
[17] Guillaume Fritz, Jean-Jacques Sinou, Jean-Marc Duffal, and Louis Jézéquel. Investigation of the relationship between damping and mode-coupling patterns in case of brake squeal. *Journal of Sound and Vibration*, 307(3-5):591–609, 2007. Publisher: Elsevier.
[18] J.-J. Sinou, Fabrice Thouverez, and Louis Jezequel. Analysis of friction and instability by the centre manifold theory for a non-linear sprag-slip model. *Journal of Sound and Vibration*, 265(3):527–559, 2003. Publisher: Elsevier.
[19] Daniel Hochlenert, Gottfried Spelsberg-Korspeter, and Peter Hagedorn. Friction Induced Vibrations in Moving Continua and Their Application to Brake Squeal. *Journal of Applied Mechanics*, 74(3):542–549, May 2007.
[20] Daniel Hochlenert. Nonlinear stability analysis of a disk brake model. *Nonlinear Dyn*, 58(1-2):63–73, October 2009.
[21] Utz von Wagner, Daniel Hochlenert, and Peter Hagedorn. Minimal models for disk brake squeal. *Journal of Sound and Vibration*, 302(3):527–539, 2007. Publisher: Elsevier.
[22] D Sinclair and N.J Manville. Frictional Vibrations. *Journal of Applied Mechanics*, pages 207–213, 1955.
[23] R. A. Ibrahim. Friction-Induced Vibration, Chatter, Squeal, and Chaos—Part II: Dynamics and Modeling. *Applied Mechanics Reviews*, 47(7):227–253, July 1994.
[24] R. A. Ibrahim. Friction-Induced Vibration, Chatter, Squeal, and Chaos—Part I: Mechanics of Contact and Friction. *Applied Mechanics Reviews*, 47(7):209–226, July 1994.
[25] J.T. Oden and J.A.C. Martins. Models and computational methods for dynamic friction phenomena. *Computer Methods in Applied Mechanics and Engineering*, 52(1-3):527–634, September 1985.
[26] Chao Gao, Doris Kuhlmann-Wilsdorf, and David D. Makel. Fundamentals of stick-slip. *Wear*, 162-164:1139–1149, April 1993.
[27] S.S. Antoniou, A. Cameron, and C.R. Gentle. The friction-speed relation from stick-slip data. *Wear*, 36(2):235–254, February 1976.
[28] E Rabinowicz. The Intrinsic Variables affecting the Stick-Slip Process. *Proc. Phys. Soc.*, 71(4):668–675, April 1958.
[29] A.K. Banerjee. Influence of kinetic friction on the critical velocity of stick-slip motion. *Wear*, 12(2):107–116, August 1968.
[30] James H. Dieterich. Time-dependent friction and the mechanics of stick-slip. *PAGEOPH*, 116(4-5):790–806, 1978.
[31] Chao Gao, Doris Kuhlmann-Wilsdorf, and David D. Makel. The dynamic analysis of stick-slip motion. *Wear*, 173(1-2):1–12, April 1994.
[32] James D. Byerlee and W. F. Brace. Stick slip, stable sliding, and earthquakes-Effect of rock type, pressure, strain rate, and stiffness. *J. Geophys. Res.*, 73(18):6031–6037, September 1968.
[33] Giuseppe Capone, Vincenzo D'Agostino, Sergio Della Valle, and Domenico Guida. Influence of the variation between static and kinetic friction on stick-slip instability. *Wear*, 161(1):121–126, April 1993.
[34] Giuseppe Capone, Vincezo D'agostino, Sergio della Valle, and Domenico Guida. Stick-slip instability analysis. *Meccanica*, 27(2):111–118, June 1992.
[35] R. T. Spurr. A Theory of Brake Squeal. *Proceedings of the Institution of Mechanical Engineers: Automobile Division*, 15(1):33–52, January 1961.
[36] R. P. Jarvis and B. Mills. Vibrations Induced by Dry Friction. *Proceedings of the Institution of Mechanical Engineers*, 178(1):847–857, June 1963.
[37] S. W. E. Earles and C. K. Lee. Instabilities Arising From the Frictional Interaction of a Pin-Disk System Resulting in Noise Generation. *Journal of Engineering for Industry*, 98(1):81–86, February 1976.
[38] A. F. D'souza and A. H. Dweib. Self-excited vibrations induced by dry friction, part 2: Stability and limit-cycle analysis. *Journal of Sound and Vibration*, 137(2):177–190, 1990. Publisher: Elsevier.
[39] A. H. Dweib and A. F. D'Souza. Self-excited vibrations induced by dry friction, part 1: experimental study. *Journal of Sound and Vibration*, 137(2):163–175, 1990. Publisher: Elsevier.
[40] Alexy Mercier, Louis Jezequel, Sébastien Besset, Abdelbasset Hamdi, and Jean-Frédéric Diebold. Nonlinear analysis of the friction-induced vibrations of a rotor-stator system. *Journal of Sound and Vibration*, 443:483–501, March 2019.
[41] Alexy Mercier, Louis Jézéquel, Sébastien Besset, Abdelbasset Hamdi, and Jean-Frédéric Diebold. Studies on detachment non-linearity at the rotor-stator interface. *Journal of Sound and Vibration*, 468:115084, March 2020.

- The modeling of geometric imperfections (gap, center distance, inclination angle) in systems with self-sustaining vibrations (system consists of a stationary part and a rotating part with friction), shows an important influence on the stability of the system.

- **Alexy MERCIER** : Conceptualization, Methodology, Software, Validation, Writing - Original Draft, Writing - Review & Editing.

- **Louis JEZEQUEL**: Conceptualization, Methodology, Software, Validation.

Declaration of interests

☒ The authors declare that they have no known competing financial interests or personal relationships that could have appeared to influence the work reported in this paper.

☐The authors declare the following financial interests/personal relationships which may be considered as potential competing interests: